Chapter 14
Propagation Effects: Ionized Media

Three distinct ionized media, or plasmas, affect the propagation of radio signals passing through them: the Earth's ionosphere; the interplanetary medium, also known as the solar wind; and the interstellar medium of our Galaxy. The effects of scattering in other galaxies or in the media between galaxies are not usually important. There are several essential differences between neutral and ionized media with regard to propagation. For neutral media, the index of refraction is greater than unity and is unaffected by magnetic fields. In ionized media, the index of refraction is less than unity and is strongly affected by magnetic fields. Most plasma phenomena scale as ν^{-2}, and their effects can be avoided or mitigated, if desired, by observations at high frequency. Absorption plays an important role in neutral media but very little in ionized media since most radio astronomical observations occur at frequencies far above the plasma frequency. Descriptions of scattering phenomena in both types of media are based on Kolmogorov theory. However, the situation in the neutral troposphere is greatly simplified because the turbulent layer lies close to the observer, and only phase fluctuations develop. The ionized media lie far from the observer, and both phase and amplitude fluctuations are often present in the wavefront when it reaches the observer.

14.1 Ionosphere

The ionosphere has been studied extensively since the pioneering experiments of Appleton and Barnett (1925) and Breit and Tuve (1926). The literature on the subject is vast. Magneto-ionic propagation theory relevant to the ionosphere is treated in depth by Ratcliffe (1962) and Budden (1961); the general physics and chemistry of the ionosphere is described by Schunk and Nagy (2009); and an excellent general treatment of ionospheric propagation is given by Davies (1965). Reviews of particular relevance to radio astronomy can be found in Evans and Hagfors

A.R. Thompson, J.M. Moran, and G.W. Swenson Jr., *Interferometry and Synthesis in Radio Astronomy*, Astronomy and Astrophysics Library,
DOI 10.1007/978-3-319-44431-4_14

Table 14.1 Maximum likely values of ionospheric effects at 100 MHz for a zenith angle[a] of 60°

Effect	Maximum[b] (Daytime)	Minimum[c] (Night)	Frequency dependence
Faraday rotation	15 rotations	1.5 rotations	ν^{-2}
Group delay	12 μs	1.2 μs	ν^{-2}
Excess (phase) path length	3500 m	350 m	ν^{-2}
Phase change	7500 rad	750 rad	ν^{-1}
Phase stability (peak to peak)	$\pm$150 rad	$\pm$15 rad	ν^{-1}
Frequency stability (rms)	$\pm$0.04 Hz	$\pm$0.004 Hz	ν^{-1}
Absorption (in D and F regions)	0.1 dB[d]	0.01 dB	ν^{-2}
Refraction (ambient)	0.05°	0.005°	ν^{-2}
Isoplanatic patch	–	$\sim$5°	ν

Adapted from Evans and Hagfors (1968).
[a]For values of parameters at the zenith, divide numbers (except refraction) by $\sec z_i$, which is approximately 1.7 [see Eq. (14.14)]. For typical (rather than maximum) parameters, divide numbers by 2.
[b]Total electron content = 5×10^{17} m^{-2}.
[c]Total electron content = 5×10^{16} m^{-2}.
[d]1 dB = 0.230 nepers.

(1968) and Hagfors (1976). Beynon (1975) gives interesting historical anecdotes on the early development of ionospheric research. In this section, we treat only those aspects of the ionosphere that have a deleterious effect on interferometric observations. Table 14.1 gives the magnitude of various propagation effects for the daytime and nighttime ionosphere. Most of these effects scale as ν^{-2}, and they can be minimized by observing at higher frequencies. For small zenith angles, the magnitude of the ionospheric excess path typically equals that of the neutral atmosphere at approximately 2 GHz, but the frequency of this equality can vary from about 1 to 5 GHz. Thus, at 20 GHz and small zenith angles, the ionospheric excess path length is typically only 1% of the tropospheric excess path length. However, at very large zenith angles, i.e., near the horizon, the effects are equal at about 300 MHz.

14.1.1 Basic Physics

The ionization of the upper atmosphere is caused by the ultraviolet radiation from the Sun. Typical daytime and nighttime vertical profiles of the electron density are shown in Fig. 14.1. The electron distribution and the total electron content vary also with geomagnetic latitude, time of year, and sunspot cycle. There are also substantial winds, traveling disturbances, and irregularities in the ionosphere. The ionosphere is

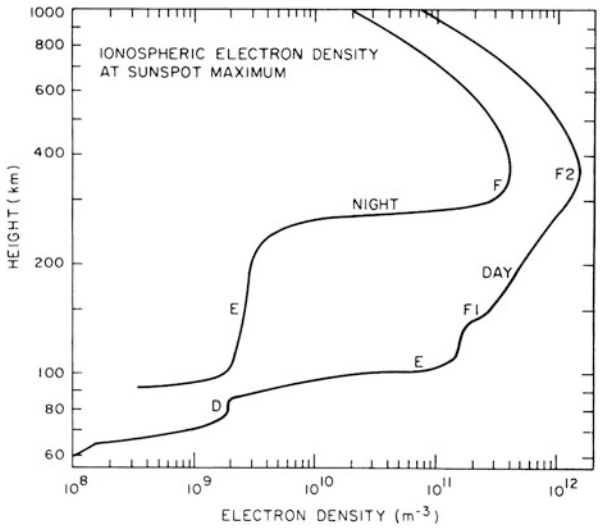

Fig. 14.1 Idealized electron density distribution in the Earth's ionosphere. The curves indicate the densities to be expected at sunspot maximum in temperate latitudes. Peak sunspot activity occurs at 11-year intervals, most recently peaking in 2001 (cycle 23) and $\sim$ 2012 (cycle 24). Cycle 24 was about a year late and rather weak [see Janardhan et al. (2015)]. From J. V. Evans and T. Hagfors, *Radar Astronomy*, 1968. © McGraw-Hill Education.

permeated by the quasi-dipole magnetic field of the Earth. Propagation is governed by the theory of waves in a magnetized plasma with collisions.

We derive some of the fundamental properties of the ionosphere related to the propagation of electromagnetic waves by considering elementary cases. First, consider a plane monochromatic wave of linear polarization that propagates through a uniform plasma of electron density n_e, where the magnetic field and collisions between particles can be neglected. The electrons oscillate with the electric field, but the protons, because of their greater mass, remain relatively unperturbed. The index of refraction can be found by calculating either the induced current or the dipole moment. Either method yields the same result. We use the latter method, as we did when considering the index of refraction of water vapor using the bound oscillator model in Sect. 13.1.4. The equation of motion of a free electron in the plasma is

$$m\ddot{\mathbf{x}} = -e\mathbf{E}_0 e^{-j2\pi\nu t} , \tag{14.1}$$

where m, e, and $\mathbf{x}$ are the mass, charge *magnitude*, and displacement of the electron, and $\mathbf{E}_0$ and ν are the amplitude and frequency of the electric field $\mathbf{E}$ of the incident wave. The magnetic field of the plane wave has negligible influence on the electrons as long as the electron velocity is much less than c, and the electric field has negligible influence on the motion of the protons. The steady-state solution to

Eq. (14.1) is

$$\mathbf{x} = \frac{e}{(2\pi\nu)^2 m}\mathbf{E}_0 e^{-j2\pi\nu t} . \tag{14.2}$$

Note that the induced current density is $\mathbf{i} = n_e e\dot{\mathbf{x}}$, where $\dot{\mathbf{x}}$, the velocity of the particle, is 90° out of phase with the driving electric field. Thus, the work done by the wave on the particles, which is $\langle \mathbf{i} \cdot \mathbf{E} \rangle$, is zero, and the wave propagates without loss, as expected, since Eq. (14.1) has no dissipative terms. The dipole moment per unit volume $\mathbf{P}$ is equal to $n_e e\mathbf{x}_0$, where $\mathbf{x}_0$ is the amplitude of oscillation. The dielectric constant ε is $1 + (\mathbf{P}/\mathbf{E}_0)/\epsilon_0$, where ϵ_0 is the permittivity of free space, so that

$$\varepsilon = 1 - \frac{n_e e^2}{4\pi^2 \nu^2 \epsilon_0 m} . \tag{14.3}$$

The dielectric constant is real and less than unity because the induced dipole is 180° out of phase with the driving field.

The index of refraction n is equal to the square root of ε, and in this case is real, so

$$n = \sqrt{1 - \frac{\nu_p^2}{\nu^2}} , \tag{14.4}$$

where

$$\nu_p = \frac{e}{2\pi}\sqrt{\frac{n_e}{\epsilon_0 m}} \simeq 9\sqrt{n_e} \text{ (Hz)} , \tag{14.5}$$

and n_e is in m^{-3}. ν_p is known as the *plasma frequency*, which is also the natural frequency of mechanical oscillations in the plasma [see, e.g., Holt and Haskell (1965)]. The plasma frequency of the ionosphere (see Fig. 14.1) is usually less than 12 MHz. Waves normally incident on a plasma with frequencies below ν_p are perfectly reflected. The phase velocity of a wave with $\nu > \nu_p$ in the plasma is c/n, which is greater than c, and the group velocity of a wave packet is cn, which is less than c.

Now consider a plasma with a static magnetic field $\mathbf{B}$ in the direction of propagation of the plane wave. The vector equation of motion of an electron, called the Lorentz equation, is

$$m\dot{\mathbf{v}} = -e\left[\mathbf{E} + \mathbf{v} \times \mathbf{B}\right] , \tag{14.6}$$

where $\mathbf{v}$ is the vector velocity. Let the incident field be a circularly polarized wave. If $\mathbf{B}$ is zero, the particle will follow the tip of the electric field vector and move in a circular orbit. If $\mathbf{B}$ is nonzero, the sum of the $\mathbf{v} \times \mathbf{B}$ force term, which will be in the radial direction, and the electric force term must be balanced by centripetal

acceleration. Thus, there is a basic anisotropy in the plasma depending on whether the wave is right or left circularly polarized, since the sign of the $\mathbf{v} \times \mathbf{B}$ term changes between the two cases. The radius R_e of the circular orbit of the electron is derived from the balance-of-forces equation $eE_0 \pm evB = mv^2/R_e$, where the scalar velocity $v = 2\pi\nu R_e$, B is the magnitude of the magnetic field, and the upper and lower signs refer to left and right circular polarization, respectively. Thus, we obtain

$$R_e = \frac{eE_0}{4\pi^2 m\nu^2 \mp 2\pi\nu eB} . \tag{14.7}$$

Following the same procedure as the one described below Eq. (14.2), we find that the index of refraction is given by the equation

$$n^2 = 1 - \frac{\nu_p^2}{\nu(\nu \mp \nu_B)} , \tag{14.8}$$

where ν_B is the gyrofrequency, or cyclotron frequency, given by

$$\nu_B = \frac{eB}{2\pi m} . \tag{14.9}$$

The gyrofrequency is the frequency at which an electron would spiral around a magnetic field line in the absence of any electromagnetic radiation. In the absence of damping, R_e would go to infinity if the applied electric field frequency were ν_B. The gyrofrequency of the Earth's magnetic field in the ionosphere ($\sim 0.5 \times 10^{-4}$ tesla) is about 1.4 MHz.

Equation (14.8) gives the index of refraction for the case of a longitudinal magnetic field, that is, where the field is parallel to the direction of wave propagation. The solution for the transverse case is different. The solution for the quasi-longitudinal case is obtained by replacing B with $B\cos\theta$, where θ is the angle between the propagation vector and the direction of the magnetic field. The quasi-longitudinal solution is applicable when the angle θ is less than that specified by the inequality (Ratcliffe 1962)

$$\frac{1}{2}\sin\theta\tan\theta < \frac{\nu^2 - \nu_p^2}{\nu\nu_B} . \tag{14.10}$$

When $\nu > 100$ MHz, $\nu_p \simeq 10$ MHz, and $\nu_B \simeq 1.4$ MHz, the quasi-longitudinal solution is valid for $|\theta| < 89°$, or virtually all cases of interest. Therefore, to a high accuracy, when $\nu \gg$ (ν_p and ν_B), we can expand Eq. (14.8) to obtain

$$n \simeq 1 - \frac{1}{2}\frac{\nu_p^2}{\nu^2} \mp \frac{1}{2}\frac{\nu_p^2\nu_B}{\nu^3}\cos\theta , \tag{14.11}$$

where we neglect terms in ν^4 and higher order. For propagation in the direction of **B**, the index of refraction is lower for a left circularly polarized wave than for a right circularly polarized wave.

The difference in the index of refraction for right and left circularly polarized waves leads to the important phenomenon of Faraday rotation, whereby a linearly polarized wave has its plane of polarization rotated as it propagates through the plasma. A linearly polarized wave with position angle ψ can be decomposed into right and left circularly polarized waves of equal amplitude and phase difference 2ψ. The phase of the two circular waves as they propagate in the y direction through a plasma is $2\pi\nu n_r y/c$ and $2\pi\nu n_\ell y/c$, where n_r and n_ℓ are the indices of refraction for the right circular and left circular modes, respectively. The phase difference between the waves is $2\pi\nu(n_r - n_\ell)y/c$. From Eq. (14.11), $n_r - n_\ell = \nu_p^2 \nu_B \nu^{-3} \cos\theta$, so it is clear that the plane of polarization is rotated by the angle

$$\Delta\psi = \frac{\pi}{c\nu^2} \int \nu_p^2 \nu_B \cos\theta \, dy \, , \tag{14.12}$$

where ν_p, ν_B, and θ may be functions of y.

For constant magnetic field and electron density, Eq. (14.12) can be written

$$\Delta\psi = 2.6 \times 10^{-13} n_e B \lambda^2 L \cos\theta \, , \tag{14.13}$$

where $\Delta\psi$ is in radians, n_e is in m^{-3}, B is in tesla and is positive when the field is pointed toward the observer, λ is the wavelength in meters, and L is the path length in meters. A magnetic field pointed toward the observer causes the position angle to increase (i.e., a counterclockwise rotation of the plane of polarization of incident radiation as viewed from the surface of the Earth).

14.1.2 Refraction and Propagation Delay

The situation with ionospheric refraction is different from that of tropospheric refraction. The latter occurs in a layer within about 10 km from the ground, and most effects can be understood, at least to first order, with a model of a plane-parallel medium. Since the index of refraction is slightly larger than unity, incoming rays are bent toward the zenith. In contrast, the layers responsible for ionospheric refraction occur several hundred kilometers above the surface, as shown in Fig. 14.2. If the ionosphere were modeled as a plane-parallel layer, then an incoming ray at a certain zenith angle would be bent away from the normal upon entering the layer and then bent back by an equal amount when exiting below. In this case, there would be no net change in the zenith angle. However, the Earth's curvature, in combination with the index of refraction of less than unity, results in a net deflection toward the zenith, the same sense as for tropospheric refraction. A concept that is especially important

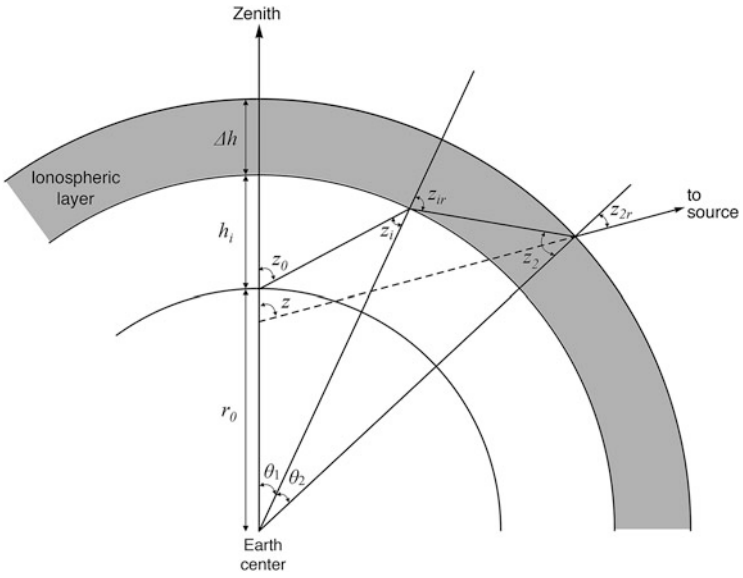

Fig. 14.2 Diagram of a ray passing through a homogeneous but exaggerated ionospheric layer from height h_i to $h_i + \Delta h$. Because of the curvature of the Earth, $z_{ir} = z_2 + \theta_2 \neq z_2$, the net bending angle $\Delta z = z - z_0$ is positive, as it is for the troposphere (see Appendix 14.1 for a derivation of Δz for this single-layer model). Note that if $z_2 > 90$, there will be total internal reflection, and the ray will not reach the Earth's surface. The effect of this internal reflection condition on the effective horizon is also discussed in Appendix 14.1. For the exaggerated case shown, $z_0 = 60°$, $n = 0.8$, and $z = 63°$. For a case with more realistic parameters, see Appendix 14.1.

in the context of all-sky or very-wide-field imaging is that the static ionosphere acts like an achromatic spherical lens that bends incoming rays toward the zenith (Vedantham et al. 2014).

To understand ionospheric refraction, consider a ray passing through a simple ionized layer as shown in Fig. 14.2. Note that the zenith angle of the ray at the bottom of the ionosphere is rather different than the zenith angle at the observer. That is, with the law of sines,

$$z_i = \sin^{-1}\left[\left(\frac{r_0}{r_0 + h_i}\right)\sin z_0\right] . \tag{14.14}$$

We can apply the law of sines to the triangle involving the upper boundary of the layer, as well as Snell's law, to obtain the bending angle of interest, $\Delta z = z - z_0$, where $z = z_{2r} + \theta_1 + \theta_2$ and z_{2r}, θ_1, and θ_2 are defined in Fig. 14.2. Δz is always ≥ 0. The details of the calculation of Δz are given in Appendix 14.1.

The case of a radially stratified ionosphere can be handled by rewriting Eq. (13.27) in the form (see Sukumar 1987, for details) as

$$\Delta z = \frac{A \sin z_0}{r_0} \frac{1}{\nu^2} \int_0^\infty \frac{\left[1 + \frac{h}{r_0}\right] n_e(h) dh}{\left[\left(1 + \frac{h}{r_0}\right)^2 - \sin^2 z_0\right]^{3/2}} , \tag{14.15}$$

where r_0 is the radius of the Earth, $n_e(h)$ is the profile of the electron density as a function of height, h, and $A = e^2/8\pi^2 m\varepsilon_0$. Note that $\nu_p^2 = An_e$ [see Eq. (14.5], so that Eq. (14.15) could be written as a vertical distribution of ν_p. Note also that $\Delta z = 0$ in the zenith direction and would go to zero for r_0 approaching infinity, as expected. Since $h \ll r_0$, for $z_0 \ll 1$, the deflection is approximately

$$\Delta z = \frac{A \sin z_0}{r_0} \frac{1}{\nu^2} \int_0^h n_e(h)\, dh . \tag{14.16}$$

The ionosphere can be modeled to reasonable accuracy with a parabolic electron density distribution of the form

$$n_e(h) = n_{e0} \left[1 - \frac{2(h - h_m)^2}{\Delta h^2}\right] , \tag{14.17}$$

as described by Bailey (1948) for $|h - h_m| \leq 1/\sqrt{2}$, and where h_m is the height of the peak of the electron density, n_{e0}, and Δh is the thickness of the layer. In this case, the bending is approximately given by

$$\Delta z = \frac{\Delta h \sin z}{3r_0} \left(\frac{\nu_p}{\nu}\right)^2 \left(1 + \frac{h_m}{r_0}\right) \left(\cos^2 z + \frac{2h_m}{r_0}\right)^{-3/2} . \tag{14.18}$$

The excess path length (see Eqs. 13.4 and 13.5) in the zenith direction can be calculated using Eqs. (14.5) and (14.11) with the assumption that $\nu \gg (\nu_p$ and $\nu_B)$. The result is

$$\mathcal{L}_0 \simeq -\frac{1}{2} \int_0^\infty \left[\frac{\nu_p(h)}{\nu}\right]^2 dh \simeq -\frac{40.3}{\nu^2} \int_0^\infty n_e(h)\, dh , \tag{14.19}$$

where ν is in hertz and $n_e(h)$ and $\nu_p(h)$ are the electron density (m^{-3}) and plasma frequency as a function of height. The integral of electron density over height in Eq. (14.19) is called the *total electron content* (TEC) or *column density*. The excess path corresponds to a phase delay and is negative for the ionosphere. If we approximate the ionosphere by a thin layer at height h_i, then the excess path length will vary as the secant of the zenith angle of the ray as it passes through the layer. Thus,

$$\mathcal{L} \simeq \mathcal{L}_0 \sec z_i , \tag{14.20}$$

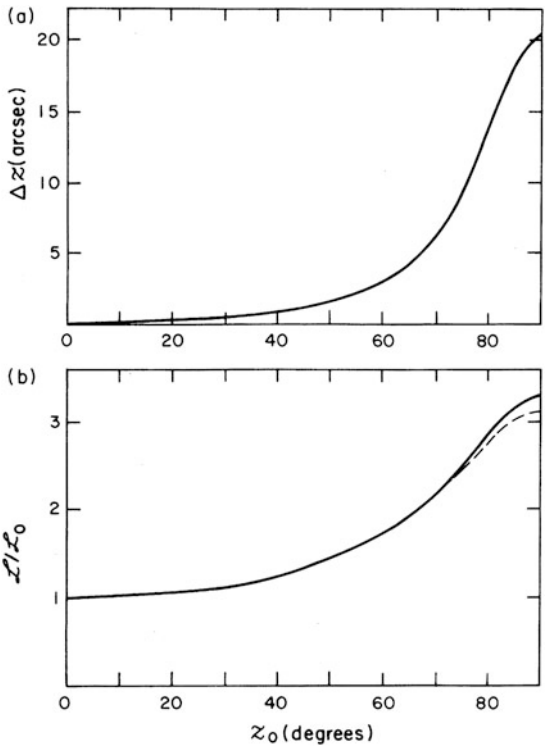

Fig. 14.3 (**a**) Ionospheric bending angle vs. zenith angle at 1000 MHz from a ray-tracing calculation for the daytime electron density profile in Fig. 14.1. The bending predicted by Eq. (14.18), with parameters $\nu_p = 12$ MHz, $h_i = 350$ km, $\Delta h = 225$ km, and $r_0 = 6370$ km, differs from the curve shown by no more than 5%. (**b**) Normalized ionospheric excess path length vs. zenith angle for the same electron density profile from a ray-tracing calculation (solid curve) and from Eq. (14.20) (dashed curve). The total electron content is 6.03×10^{17} m^{-2}, and the excess path length at the zenith is 24.3 m. The bending and excess path length scale as ν^{-2}. The function forms are rather different from those of the troposphere shown in Fig. 13.6.

where z_i (see Fig. 14.2) is given by Eq. (14.14). Because of the diurnal variation in n_e, it may be important to use the ionospheric penetration coordinates (defined by θ_1 and θ_2 in Fig. 14.2) to calculate $\mathcal{L}_0$ in Eq. (14.19) for a particular site.

When $z = 90°$ and $h_i = 400$ km, $\sec z_i$ is only ~ 3. The secant law provides a reasonable model for estimating the excess ionospheric path length. A more complex model can be found in Spoelstra (1983)). Plots of Δz from ray tracing and $\mathcal{L}$ obtained from Eqs. (14.18) and (14.20) as well as from actual ray-tracing calculations are shown in Fig. 14.3.

In some applications, it is necessary to correct the measurements of fringe frequency for the effects of ionospheric delay. The ionospherically induced frequency shift at an antenna is $(\nu/c)d\mathcal{L}/dt$. The time rate of change in excess path length $d\mathcal{L}/dt$ has two components: one caused by the time rate of change of zenith angle dz/dt, and the other caused by the time rate of change of $\mathcal{L}_0$, $d\mathcal{L}_0/dt$. At many times, especially near sunrise and sunset, the latter term may dominate (Mathur et al. 1970; Hagfors 1976).

14.1.3 Calibration of Ionospheric Delay

The excess ionospheric path length must be calibrated as accurately as possible in experiments involving precise determination of source positions or baselines. Three approaches are possible. In the first approach, models of the ionosphere can be constructed that depend on parameters such as geomagnetic latitude, solar time, season, and solar activity. Two such models are the International Reference Ionosphere (IRI) (Bilitza 1997) and the Parametrized Ionosphere Model (PIM) (Daniell et al. 1995).

In the second approach, estimates of the total electron content can be obtained from measurements of the dual-frequency transmissions from the Global Positioning System (GPS) (Ho et al. 1997; Mannucci et al. 1998). GPS has replaced the more traditional methods such as ionosondes, Faraday rotation of satellite signals, and incoherent backscatter radar (Evans 1969). The usefulness of GPS for phase correction of array data has been tested at the VLA (Erickson et al. 2001). Four GPS receivers were installed, one at the array center, and one at the end of each arm. The GPS receiver measured the TEC along lines of sight to the GPS satellite. When compared with interferometric phases at 330 MHz, the GPS system was effective in predicting wavefront slopes from large-scale structures ($> 1,000$ km) in the ionosphere. GPS methods have also been used in the calibration of VLBI observations (e.g., Ros et al. 2000).

In the third approach, the differential path length effects can be virtually eliminated for unresolved sources by making astronomical observations simultaneously at two widely separated frequencies, ν_1 and ν_2. If the interferometer phases are ϕ_1 and ϕ_2 at the two frequencies, then the quantity

$$\phi_c = \phi_2 - \left(\frac{\nu_1}{\nu_2}\right)\phi_1 \tag{14.21}$$

will preserve source position information and be substantially free of ionospheric delay effects. This technique will correct for the effects of all plasmas along the line of sight, not only the ionosphere. A small residual error remains because of higher-order frequency terms in the index of refraction and because the rays at the two frequencies traverse slightly different paths through the ionosphere. Dual-frequency observations are widely used in astrometric radio interferometry where source structure can be neglected [see, e.g., Sect. 12.6; Fomalont and Sramek (1975); Kaplan et al. (1982); Shapiro (1976)]. Note that the difference in TEC along the ray paths to the interferometer elements can be estimated from measurement of $\phi_2 - (\nu_2/\nu_1)\phi_1$. Similar dual-frequency systems can be employed for the transfer of a local oscillator reference to a space-based VLBI station [see, for example, Moran (1989) and Sect. 9.10].

14.1.4 Absorption

Absorption in the ionosphere is caused by collisions of electrons with ions and neutral particles. At frequencies much greater than ν_p, the power absorption coefficient is

$$\alpha = 2.68 \times 10^{-7} \frac{n_e \nu_c}{\nu^2} \ (\mathrm{m}^{-1}) \ , \tag{14.22}$$

where ν_c is the collision frequency and n_e is in m^{-3}. The collision frequency in hertz is approximately

$$\nu_c \simeq 6.1 \times 10^{-9} \left(\frac{T}{300} \right)^{-3/2} n_i + 1.8 \times 10^{-14} \left(\frac{T}{300} \right)^{1/2} n_n \ , \tag{14.23}$$

where n_i is the ion density and n_n is the neutral particle density, both in m^{-3} (Evans and Hagfors 1968). Numerical values of absorption are listed in Table 14.1. Radiometric measurements of both electron temperature and opacity have been made by Rogers et al. (2015).

14.1.5 Small- and Large-Scale Irregularities

The small-scale irregularities in the electron density distribution introduce random changes in the wavefront of a passing electromagnetic wave. As a consequence, fluctuations in fringe amplitude and phase can be readily observed with an interferometer at frequencies below a few hundred megahertz. In the early days of radio astronomy, signals from Cygnus A and other compact sources were observed to fluctuate on timescales of 0.1–1 min. At first, these fluctuations were thought to be intrinsic to the sources (Hey et al. 1946), but later observations with spaced receivers showed that the fluctuations were uncorrelated for receiver separations of more than a few kilometers (Smith et al. 1950). This result led to the conclusion that irregularities in the ionosphere were perturbing the cosmic signals. The predominant scale sizes in the ionization irregularities were found to be a few kilometers or less. The timescale of the fluctuations indicates that ionospheric wind speeds are in the range of 50–300 m s^{-1}. The effects of these fluctuations have been studied extensively at frequencies between about 20 and 200 MHz and have been observed at frequencies as high as 7 GHz (Aarons et al. 1983). An early example of the fluctuations seen in interferometer measurements is given in Fig. 14.4. Hewish (1952), Booker (1958), and Lawrence et al. (1964) reviewed the early results and techniques. A comprehensive review of theory and observations of ionospheric fluctuations can be found in Crane (1977), Fejer and Kelley (1980), and Yeh and Liu (1982), and summaries of global morphology can be found in Aarons (1982) and

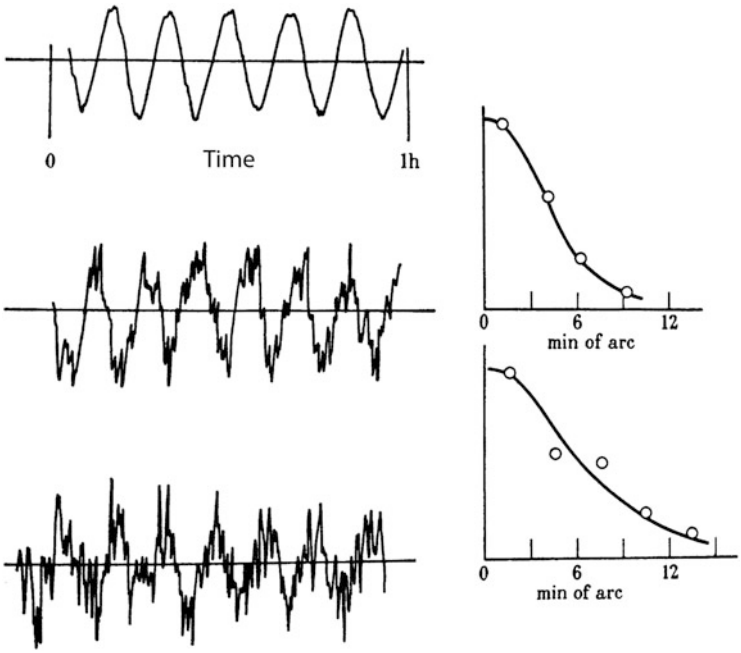

Fig. 14.4 (**left**) Typical records of the correlator output on three occasions from a phase-switching interferometer at Cambridge, England, having a 1-km baseline and operating at a wavelength of 8 m. The irregular responses are caused by disturbances in the ionosphere. (**right**) Probability distributions of the angle of arrival deduced from the zero crossings of the correlator response. Reprinted with permission of and © the Royal Society, conveyed through Copyright Clearance Center Inc. From Hewish (1952).

Aarons et al. (1999). Measurements with the GPS can be very useful in monitoring ionospheric fluctuations [e.g., Ho et al. (1996), Pi et al. (1997)]. The effects of ionospheric scintillation on a synthesis telescope have been described by Spoelstra and Kelder (1984). Loi et al. (2015a) report extensive measurements of ionospheric-induced position wander in sources at 150 MHz, and Loi et al. (2015b) demonstrated a parallax technique for determining the height of the perturbing layer. In Sect. 14.2, we discuss a theory of scintillation, which can be applied to the ionosphere as well as to the interplanetary and interstellar media.

Large-scale variations in the electron density integrated along the line of sight are caused by traveling ionospheric disturbances (TIDs). TIDs, which are manifestations of acoustic-gravity waves in the upper atmosphere, are quasi-periodic, large-scale perturbations in electron density. The atmosphere has a natural buoyancy, so that a parcel of gas displaced vertically and released will oscillate at a frequency known as the Brunt–Väisälä, or buoyancy, frequency. This frequency is about 0.5–2 mHz (periods of 10–20 min) at ionospheric heights. For waves with frequencies above the buoyancy frequency, the restoring force is pressure (acoustic wave), and for waves with frequencies below the buoyancy frequency, the restoring

force is gravity (gravity wave). Hunsucker (1982) and Hocke and Schlegel (1996) have reviewed the literature on acoustic-gravity waves. There are many potential sources of TIDs, including auroral heating, severe weather fronts, earthquakes, and volcanic eruptions. Medium-scale TIDs have scale lengths of 100–200 km and timescales of 10–20 min and cause a variation in TEC of 0.5–5%. Such TIDs are present for a substantial fraction of the time. Large-scale TIDs, which are relatively uncommon, have scale lengths of 1000 km and timescales of hours and can cause variations in TEC of up to 8%. One such disturbance, excited by a volcano, was observed by VLBI (Roberts et al. 1982). A variety of ionospheric disturbances have been studied by observations of compact sources with the VLA [e.g., Helmboldt et al. (2012), Helmboldt (2014)].

14.2 Scattering Caused by Plasma Irregularities

Understanding the propagation of radiation in a random medium is an important problem in many fields. The signals from cosmic radio sources propagate through several ionized random media, including the ionized interstellar gas of our Galaxy, the solar wind, and the ionosphere. In the observer's plane, there are two effects. First, the amplitude varies with the position of the observer, which leads to temporal amplitude variations if there are relative motions among the source, scattering medium, and observer. Second, the image of the source is also distorted in a frequency-dependent manner. Much of the research in this area has been motivated by the attempt to understand the observational characteristics of pulsars [see, e.g., Gupta (2000)]. Propagation effects in the turbulent troposphere are described in Chap. 13.

14.2.1 Gaussian Screen Model

We begin the discussion by considering a simple model that serves to illustrate many features of the problem. This model was first developed by Booker et al. (1950)) to explain ionospheric scintillation and was refined by Ratcliffe (1956). Scheuer (1968) applied it to pulsar observations. The model assumes that the irregular medium is confined to a thin screen and that the irregularities (blobs) have one characteristic scale size a. Diffraction effects are neglected within the irregular medium; only the phase change imposed by the medium is considered. Diffraction is taken into account in the free-space region between the irregular medium and the receivers.

The geometric situation is shown in Fig. 14.5. The thin-screen assumption is not particularly restrictive. However, the assumption that the screen is filled with plasma blobs having one characteristic size is restrictive and distinguishes this model from the power-law model, in which a range of scale sizes is present. From Eqs. (14.5)

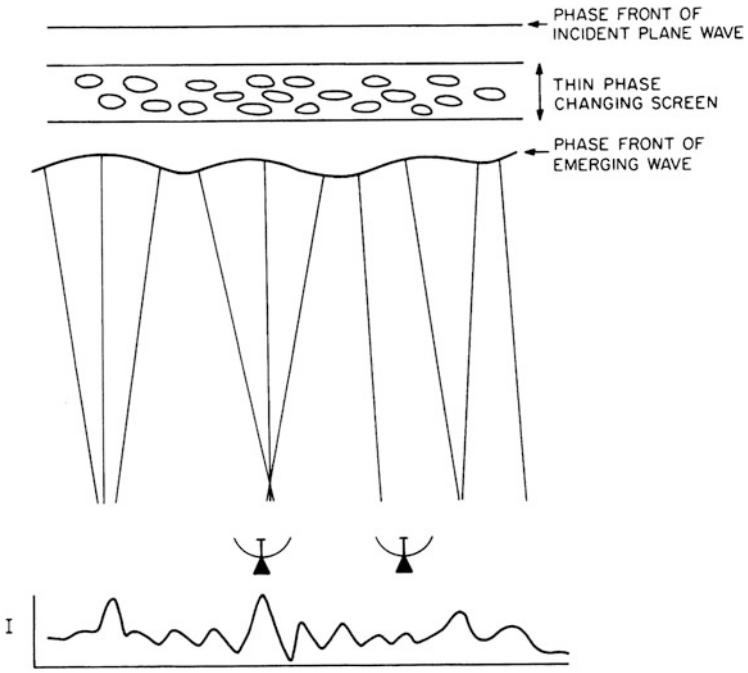

Fig. 14.5 Geometry of a thin-screen scintillation model. An initially plane wave is incident on a thin phase-changing screen. The emerging wavefront is irregular. As the wave propagates to the observer, amplitude fluctuations develop, as suggested by the crossing rays. Below the antenna is a plot of intensity vs. position along the wavefront. If there is motion between the screen and the observer, the spatial fluctuations will be observed as temporal fluctuations in the power received or the fringe visibility.

and (14.11), the index of refraction of the plasma can be written

$$n \simeq 1 - \frac{r_e n_e \lambda^2}{2\pi} \,, \tag{14.24}$$

where r_e is the classical electron radius, equal to $e^2/4\pi\epsilon_0 mc^2$ or 2.82×10^{-15} m, and the term in ν_B is neglected. Thus, the excess phase shift (a phase advance in this situation) across one blob is

$$\Delta\phi_1 = r_e \lambda a \, \Delta n_e \,, \tag{14.25}$$

where Δn_e is the excess electron density in the blob over the ambient level. If the thickness of the screen is L, then the wave will encounter about L/a blobs, and the rms phase deviation $\Delta\phi$ will be $\Delta\phi_1 \sqrt{L/a}$, or

$$\Delta\phi = r_e \lambda \, \Delta n_e \sqrt{La} \,. \tag{14.26}$$

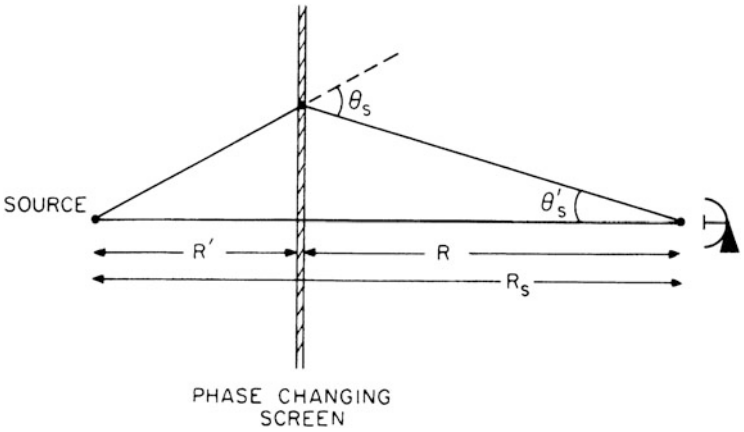

Fig. 14.6 Path of a refracted ray in the thin-screen model. The rms scattering angle, θ_s, is given by Eq. (14.27).

The wave emerging from the screen is crinkled; that is, the amplitude is unchanged, but the phase is no longer constant and has random fluctuations with rms deviation $\Delta\phi$. The wave can therefore be decomposed into an angular spectrum of waves propagating with a variety of angles. The full width of the angular spectrum, θ_s, can be estimated by imagining that the random medium consists of refracting wedges that tilt the wavefront by the amount $\pm\Delta\phi\lambda/2\pi$ over a distance a. Thus,

$$\theta_s = \frac{1}{\pi} r_e \lambda^2 \Delta n_e \sqrt{\frac{L}{a}} \,. \tag{14.27}$$

If the source is not infinitely distant, then the incident wave will not be plane. In that case, the observed scattering angle θ_s' depends on the location of the screen with respect to the source and the observer. Since θ_s and θ_s' are small angles, it follows from the geometry in Fig. 14.6 that

$$\theta_s' = \frac{R'}{R + R'} \theta_s \,, \tag{14.28}$$

where R and R' are defined in Fig. 14.6. Therefore, the effectiveness of the scattering screen is diminished if the screen is moved toward the source. This lever effect is very important in astrophysical situations. It can be used to distinguish galactic and extragalactic sources whose radiation passes through the same scattering screen (Lazio and Cordes 1998).

Amplitude fluctuations build up as the wave propagates away from the screen. If the phase fluctuations are large, $\Delta\phi > 1$, then significant amplitude fluctuations occur when rays cross (see Fig. 14.5). The critical distance beyond which

large-amplitude fluctuations are observed is

$$R_f \simeq \frac{a}{\theta_s'} \,. \tag{14.29}$$

Note that if $\Delta\phi = 2\pi$, then R_f is the distance for which the size of a blob is equal to the size of the first Fresnel zone. The random electric field distribution at the Earth, in the plane perpendicular to the propagation direction, is called the diffraction pattern. It has a characteristic correlation length d_c, given by

$$d_c \simeq \frac{\lambda}{\theta_s'} \,. \tag{14.30}$$

If the screen moves with relative velocity v_s in the direction perpendicular to the propagation direction, so that the diffraction pattern sweeps across the observer, then the timescale of variability is

$$\tau_d \simeq \frac{d_c}{v_s}\frac{R'}{R+R'} \simeq \frac{\lambda}{\theta_s v_s} \,. \tag{14.31}$$

The signal reaching the observer by traveling along the scattered ray path is delayed by an amount

$$\tau_c \simeq \frac{RR'\theta_s^2}{2c(R+R')} \tag{14.32}$$

with respect to the unscattered signal. The phase of the scattered wave is $2\pi\nu\tau_c$ with respect to the direct (unscattered) wave, and interference between these two waves causes scintillation. The bandwidth over which the relative phase changes by 2π is called the correlation bandwidth, $\Delta\nu_c$. The correlation bandwidth is the reciprocal of τ_c, and for the case $R = R'$ is

$$\Delta\nu_c \simeq \frac{8c}{R_s\theta_s^2} \,, \tag{14.33}$$

where R_s is the distance between the source and the observer. If the observations are made with a receiver of bandwidth greater than $\Delta\nu_c$, the amplitude fluctuations will be greatly reduced. Note from Eqs. (14.33) and (14.27) that $\Delta\nu_c$ varies as λ^{-4}.

Finally, if the source has two equal components separated by distance ℓ, then each component will produce the same diffraction pattern, but these patterns will be displaced at the Earth by distance $\ell R/R'$. If this distance is greater than d_c, then the diffraction pattern will be smoothed and the amplitude fluctuations reduced. Thus, if the source size is greater than a critical size θ_c, amplitude fluctuations will be sharply reduced because the diffraction patterns from the component parts overlap

and are smoothed out. From Eqs. (14.28) and (14.30), θ_c can be written as

$$\theta_c = \frac{\lambda}{R\theta_s} \,. \tag{14.34}$$

Hence, only sources of small angular diameter scintillate. In the optical regime, the analogous phenomenon is that stars twinkle, but usually planets do not. An elegant application of Eq. (14.34) was made by Frail et al. (1997) to determine the angular size of the expanding radio source associated with a gamma-ray burst. They determined that the amplitude fluctuations in the radio emission, assumed to be caused by interstellar scattering, ceased during the first weeks after the burst, indicating that the source diameter had increased beyond the critical size of 3 μas at that time.

A useful quantity is the ensemble average fringe visibility, $\mathcal{V}_m$, measured by an interferometer in the presence of scintillation. Assume that the phases ϕ_1 and ϕ_2 at two points along the phase screen, separated by distance d, are random variables with a joint Gaussian distribution with variance $\Delta\phi^2$ and normalized correlation $\rho(d)$. $\rho(d)$ is the correlation function of the phase or of the variable component of the index of refraction. The joint probability density function of the phase along the wavefront is

$$p(\phi_1, \phi_2) = \frac{1}{2\pi\,\Delta\phi^2\sqrt{1-\rho(d)^2}} \exp\left[-\frac{\phi_1^2 + \phi_2^2 - 2\rho(d)\phi_1\phi_2}{2\Delta\phi^2[1-\rho(d)^2]}\right] , \tag{14.35}$$

where $\rho(d) = \langle\phi_1\phi_2\rangle/\Delta\phi^2$, the correlation function of the phase fluctuations. The expectation of $e^{j(\phi_1-\phi_2)}$ is

$$\langle e^{j(\phi_1-\phi_2)}\rangle = \iint e^{j(\phi_1-\phi_2)}\, p(\phi_1, \phi_2)\, d\phi_1\, d\phi_2 \,, \tag{14.36}$$

which can be evaluated directly from Eq. (14.35) with the result

$$\langle e^{j(\phi_1-\phi_2)}\rangle = e^{-\Delta\phi^2[1-\rho(d)]} \,. \tag{14.37}$$

For a point source of flux density S, the ensemble average of the fringe visibility is

$$\langle\mathcal{V}_m\rangle = S\langle e^{j\phi_1}e^{-j\phi_2}\rangle \,, \tag{14.38}$$

or

$$\langle\mathcal{V}_m\rangle = Se^{-\Delta\phi^2[1-\rho(d)]} \,. \tag{14.39}$$

If the source has an intrinsic visibility $\mathcal{V}_0$, the ensemble average is

$$\langle\mathcal{V}_m\rangle = \mathcal{V}_0 e^{-\Delta\phi^2[1-\rho(d)]} \,. \tag{14.40}$$

This result was first derived by Ratcliffe (1956) and Mercier (1962). Note that the structure function of phase is $D_\phi(d) = 2\Delta\phi^2[1 - \rho(d)]$, so that Eq. (14.40) is equivalent to Eq. (13.80). In much of the early radio astronomical literature, $\rho(d)$ is assumed to be a Gaussian function

$$\rho(d) = e^{-d^2/2a^2} , \tag{14.41}$$

where the characteristic scale length a corresponds to the blob size in the discussion above. This model, called the Gaussian screen model, is probably unrealistically restrictive because there are undoubtedly many scale sizes present. In the case in which $\Delta\phi \gg 1$, $\mathcal{V}_m$ decreases rapidly as d increases, and we need consider only the situation of $d \ll a$. Then, substitution of Eq. (14.41) into Eq. (14.40) yields

$$\langle \mathcal{V}_m \rangle \simeq \mathcal{V}_0 e^{-\Delta\phi^2 d^2/2a^2} . \tag{14.42}$$

Thus, the intensity distribution of a point source observed through a Gaussian screen is a Gaussian distribution with a diameter (full width at half-maximum) of

$$\theta_s \simeq \sqrt{2\ln 2}\frac{\Delta\phi\lambda}{\pi a} = \frac{\sqrt{2\ln 2}}{\pi} r_e \lambda^2 \Delta n_e \sqrt{\frac{L}{a}} . \tag{14.43}$$

This formula for θ_s is essentially equivalent to the one given in Eq. (14.27). In the case in which $\Delta\phi \ll 1$, the normalized visibility function drops from unity to $e^{-\Delta\phi^2}$ when $d \gg a$. Therefore, the resulting intensity distribution for a point source is an unresolved core surrounded by a halo. The ratio of the flux density in the halo to the flux density in the core is $e^{\Delta\phi^2} - 1$.

14.2.2 Power-Law Model

The spectrum of fluctuations in the electron density in ionized astrophysical plasmas is normally modeled as a power law,

$$P_{ne} = C_{ne}^2 q^{-\alpha} , \tag{14.44}$$

where q is the three-dimensional spatial frequency (cycles per meter), $q^2 = q_x^2 + q_y^2 + q_z^2$, and C_{ne}^2 characterizes the strength of the turbulence. The definition of C_{ne}^2 varies in the literature, depending on whether it is used as a constant in the spectrum or in the structure function. The two-dimensional power spectrum of phase [see Eq. (14.22) for the relation between $\Delta\phi$ and Δn_e] is

$$P_\phi(q) = 2\pi r_e^2 \lambda^2 L P_{ne} . \tag{14.45}$$

Hence, from Eq. (13.104), the structure function of phase is

$$D_\phi(d) = 8\pi^2 r_e^2 \lambda^2 L \int_0^\infty [1 - J_0(qd)] P_{ne}(q) q \, dq \, . \tag{14.46}$$

For a power-law spectrum of the form of Eq. (14.44), the structure function is

$$D_\phi(d) = 8\pi^2 r_e^2 \lambda^2 C_{ne}^2 L f(\alpha) d^{\alpha-2} \, , \tag{14.47}$$

where $f(\alpha)$ is of order unity. The index α is often taken to be 11/3, which is its value for Kolmogorov turbulence, for which $f(\alpha) = 1.45$ [see Cordes et al. (1986)) for other values of $f(\alpha)$]. The ensemble average of the interferometric visibility [see Eq. (13.80)] is

$$\langle \mathcal{V} \rangle = \mathcal{V}_0 e^{-D_\phi/2} \, , \tag{14.48}$$

or

$$\langle \mathcal{V} \rangle = \mathcal{V}_0 e^{-4\pi^2 r_e^2 \lambda^2 C_{ne}^2 L f(\alpha) d^{\alpha-2}} \, . \tag{14.49}$$

The observed intensity distribution, the Fourier transform of Eq. (14.49), differs slightly from a Gaussian distribution, as can be seen in Fig. 13.11b. The scattering angle (full width at half-maximum) obtained from the width of the intensity distribution is

$$\theta_s \simeq 4.1 \times 10^{-13} (C_{ne}^2 L)^{3/5} \lambda^{11/5} \ \text{(arcsec)} \, , \tag{14.50}$$

where λ is in units of meters and $C_{ne}^2 L$ is in $\mathrm{m}^{-17/3}$. Thus, a difference between the power-law model and the Gaussian screen model is that θ_s, measured by Fourier transformation of visibility data over a range of baselines, is proportional to $\lambda^{2.2}$ in the former model and to λ^2 in the latter. Note that if $\langle \mathcal{V} \rangle$ were measured on a single baseline, that is, with d fixed, and if θ_s were estimated from comparison of the measured visibility with the visibility expected for a Gaussian intensity distribution, θ_s would appear to vary as λ^2 in both models.

Measurements of visibility must be made over sufficiently long integration times to achieve an ensemble average if Eqs. (14.48), (14.49), and (14.50) are to be valid (Cohen and Cronyn 1974). A detailed discussion of the averaging time necessary to achieve an ensemble average is given by Narayan (1992) (see also Sect. 14.4.3).

For plasmas, we can expect that the power law will hold from an inner scale q_0 to an outer scale q_1; that is, there are no fluctuations on length scales smaller than $\ell_{\text{inner}} = 1/q_1$ or larger than $\ell_{\text{outer}} = 1/q_0$. For the case in which $qd \ll 1$, that is, when the baseline is shorter than the inner length scale, the Bessel function in

Eq. (14.46) becomes $1 - q^2 r^2/4$, and the integration is straightforward, yielding

$$D_\phi(d) = \frac{2\pi^2 r_e^2 \lambda^2 L C_{ne}^2}{4-\alpha}(q_1^{4-\alpha} - q_0^{4-\alpha})\, d^2 \ . \tag{14.51}$$

This is a very important result that has two interesting consequences. First, the structure function varies as d^2 regardless of α. Second, for $\alpha < 4$, the structure function is dominated by the effect of the smallest irregularities, whereas for $\alpha > 4$, it is dominated by the effect of the largest-scale irregularities. This result also suggests an important demarcation in phenomena between plasmas with $\alpha < 4$ and those with $\alpha > 4$. The case in which $\alpha < 4$ is called Type A (shallow spectrum), and the case in which $\alpha > 4$ is called Type B (steep spectrum) (Narayan 1988).

Consider the situation in which the spectrum has three regimes:

$$\begin{aligned} P_{ne} &= C_{ne}^2 q_0^{-\alpha} \ , & q < q_0 \\ &= C_{ne}^2 q^{-\alpha} \ , & q_0 < q < q_1 \\ &= 0 \ , & q > q_1 \ . \end{aligned} \tag{14.52}$$

Substitution of Eq. (14.52) into Eq. (14.46) gives

$$\begin{aligned} D_\phi(d) &\simeq c_1 d^2 \ , & d < 1/q_1 = \ell_{\text{inner}} \\ &\simeq \left(\frac{d}{d_0}\right)^{\alpha-2} \ , & 1/q_1 < d < 1/q_0 \\ &\simeq c_2 \ , & d > 1/q_0 = \ell_{\text{outer}} \ , \end{aligned} \tag{14.53}$$

where c_1 and c_2 are constants, and we have introduced the normalization factor d_0, such that $D_\phi(d_0) = 1$, as in the discussion of the troposphere in Sect. 13.1.7. We have also assumed that $1/q_1 < d_0 < 1/q_0$. The constants needed to join the power-law segments are $c_1 = q_1^{4-\alpha} d_0^{-2}$ and $c_2 = (q_0 d_0)^{1-\alpha}$. This spectrum and structure function for the model are shown in Fig. 14.7.

14.3 Interplanetary Medium

14.3.1 Refraction

Radio waves passing near the Sun are bent by the ionization of the solar corona and the solar wind. The general characteristics of the solar corona and the solar wind can be found in Winterhalter et al. (1996). Calculation of the refraction in the extended solar atmosphere is important for the understanding of solar radio emission at low frequencies, where the bending angles are large (Kundu 1965), and for tests of the

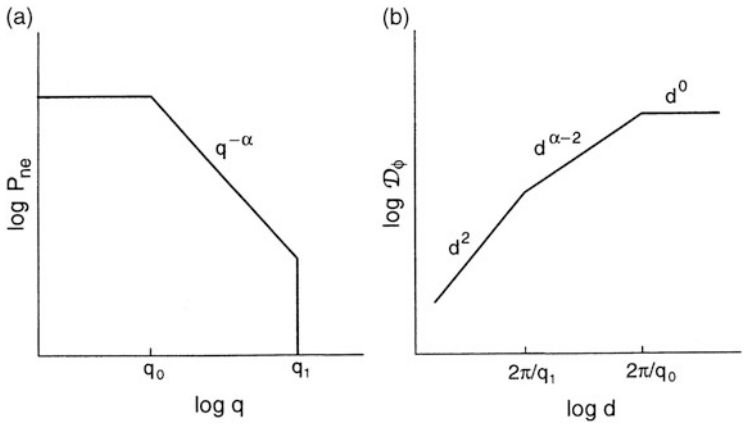

Fig. 14.7 (**a**) A model spectrum of the electron density fluctuations with inner and outer scales of spatial frequency q_0 and q_1. (**b**) The corresponding structure function of phase: see Eqs. (14.52) and (14.53). Note that $\ell_{\text{inner}} = 2\pi q_1$ and $\ell_{\text{outer}} = 2\pi/q_0$. From Moran (1989), © Kluwer Academic Publishers. With kind permission from Springer Science and Business Media.

general relativistic bending of electromagnetic radiation passing near the Sun (see Sect. 12.6).

The electron density as a function of distance from the Sun can be measured in a variety of ways. Optical observations of Thomson scattering during solar eclipses have been analyzed to give an electron density model

$$n_e = \left(1.55r^{-6} + 2.99r^{-16}\right) \times 10^{14} \ \ (\text{m}^{-3}) \ , \tag{14.54}$$

where r, the radial distance from the Sun in units of the solar radius, is less than ~4. Equation (14.54) is the well-known Allen–Baumbach formula (Allen 1947).

The electron density profile over a broad range of radii can be determined from satellites that can track the plasma frequency measured during solar radio bursts. For example, observations with the Wind spacecraft with observations from 14 MHz to a few kHz could be reasonably represented by the model

$$n_e = 3.3 \times 10^{11} r^{-2} + 4.1 \times 10^{11} r^{-4} + 8.0 \times 10^{13} r^{-6} \ \ (\text{m}^{-3}) \tag{14.55}$$

for $1.2 < r < 215$ (Leblanc et al. 1998). The value of n_e at $r = 217$ (1 AU) is 7.2×10^6 m^{-3}. This model is based on data taken near sunspot minimum, and the range of conditions is shown in Fig. 14.8. Ground-based measurements of radio sources during solar occultations (e.g., scintillations of the Crab Nebula) (Erickson 1964; Evans and Hagfors 1968) and dispersion measurements of pulsars (Counselman and Rankin 1972; Counselman et al. 1974) give about the same result as Eq. (14.55) for $r > 10$.

The angle of refraction of a ray passing near the Sun can be calculated readily for the case in which this angle is small. A ray obeys Snell's law in spherical

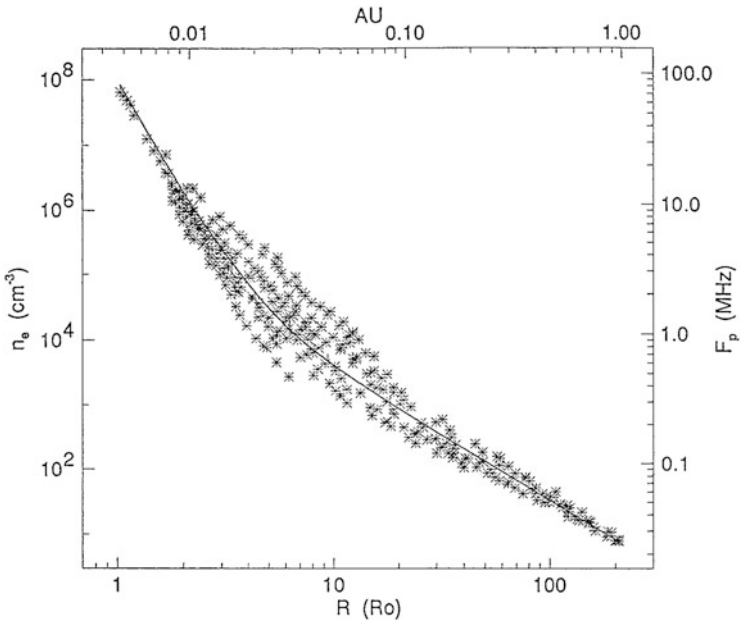

Fig. 14.8 The electron density vs. radial distance from the Sun, measured by the Wind satellite (orbiting at 1 AU) from observations of solar radio bursts. Scatter in data derived from observations at 11 epochs indicates the range of condition in the solar wind. For other data and in situ measurements, see Bougeret et al. (1984). From Leblanc et al. (1998), © *Solar Phys.* With kind permission from Springer Science and Business Media.

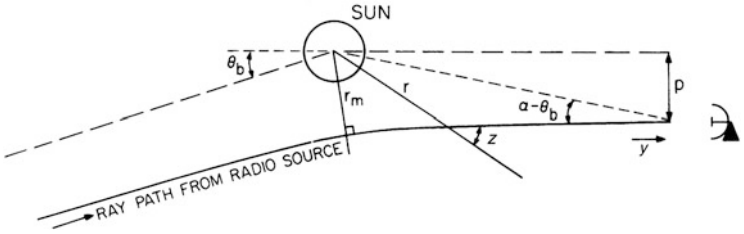

Fig. 14.9 Path of a ray passing through the ionized gas surrounding the Sun. p is the impact parameter, and α is the solar elongation angle, that is, the angle between the Sun and the source in the absence of solar bending.

coordinates, $nr\sin z$ = constant (Smart 1977), where n is the index of refraction and z is the angle between the ray and a line from the center of the Sun, as shown in Fig. 14.9. From this relation, the bending angle is found to be

$$\theta_b = \pi - 2\int_{r_m}^{\infty} \frac{dr}{r\sqrt{(nr/p)^2 - 1}}\,, \tag{14.56}$$

where r_m is the distance of closest approach of the ray to the Sun, and p is the impact parameter (see Fig. 14.9). Assume that the electron density has a single power-law distribution given by

$$n_e = n_{e0} r^{-\beta} \ , \tag{14.57}$$

where n_{e0} is the electron density in m^{-3} at one solar radius, and β is a constant. For a fully ionized solar wind, characterized by a constant mass loss rate and velocity, β is equal to 2. This case is applicable for $r \gtrsim 10$ (see Fig. 14.8). The index of refraction is obtained by substituting Eqs. (14.57) and (14.5) into Eq. (14.11) and neglecting the term in ν_B. Graphical solutions of Eq. (14.56) for large bending angles are given by Jaeger and Westfold (1950). For small bending angles, an approximate solution to Eq. (14.56) can be obtained by the use of the substitution $nr/p = \sec\theta$,

$$\theta_b \simeq 80.6\sqrt{\pi}\,\frac{n_{e0}}{\nu^2}\,\frac{\Gamma\left(\frac{\beta+1}{2}\right)}{\Gamma\left(\frac{\beta}{2}\right)} p^{-\beta} \ , \tag{14.58}$$

where p is in units of the solar radius, and Γ is the gamma function. Note that the rays are bent away from the Sun. The bending angle associated with the model in Eq. (14.55) (using only the quadratic term) is

$$\theta_b \simeq 2.4\lambda^2 p^{-2} \text{ (arcmin)} \ , \tag{14.59}$$

where λ is the wavelength in meters. For a multiple power-law model of electron density such as given in Eqs. (14.54) and (14.55), the bending angles for each component can be summed when the bending angles are small.

There is another pedagogically interesting way to determine the bending angle from the change in excess propagation path with impact parameters. The excess (phase) path for a ray passing through the corona, for the case in which the effect of ray bending can be neglected, is, from Eq. (14.19),

$$\mathcal{L} \simeq -\frac{40.3}{\nu^2}\int_{-\infty}^{\infty} n_e \, dy \ , \tag{14.60}$$

where y is measured along the ray path as shown in Fig. 14.9. For a power-law model given by Eq. (14.57), the excess path is

$$\mathcal{L} \simeq -\frac{40.3 n_{e0}}{\nu^2}\int_{-\infty}^{\infty} \frac{dy}{(p^2+y^2)^{\beta/2}} \ , \tag{14.61}$$

which can be integrated to give

$$\mathcal{L} \simeq -\frac{40.3\sqrt{\pi}}{\nu^2}\,\frac{\Gamma\left(\frac{\beta-1}{2}\right)}{\Gamma\left(\frac{\beta}{2}\right)} n_{e0} p^{1-\beta} \ . \tag{14.62}$$

The change in $\mathcal{L}$ with p describes the tilting of the wavefront and is the bending angle; hence $\theta_b \simeq d\mathcal{L}/dp$ (Bracewell et al. 1969). Differentiation of Eq. (14.62) with respect to p gives Eq. (14.58).

We mention the effect of the general relativistic bending of waves passing close to the Sun here because the phenomenon can be described classically by an effective index of refraction given by $1 + 2GM_\odot/rc^2$, where G is the gravitational constant, and $M_\odot$ is the mass of the Sun. The bending angle, for small values of p, is (Weinberg 1972)

$$\theta_{\rm GR} \simeq -1.75 p^{-1} \ \text{(arcsec)} \ . \tag{14.63}$$

The negative sign indicates that the bending is toward the Sun, which is the opposite sense of bending by interplanetary medium. Measurements of the solar general relativistic bending are discussed in more detail in Sect. 12.6.

14.3.2 Interplanetary Scintillation (IPS)

Scintillation of extragalactic radio sources due to irregularities in the solar wind was first observed by Clarke (1964) and reported by Hewish et al. (1964). Clarke was studying 88 of the 3C sources at 178 MHz with the Cambridge one-mile interferometer. She noticed that three of the sources, the only ones smaller than $2''$, showed anomalous rapid (< 1 s) scintillation, which could not be attributed to the ionosphere. They were all within 30° in angle from the Sun. Interplanetary scintillation is readily distinguishable from ionospheric scintillation, since the timescale [Eq. (14.31)] and critical source size [Eq. (14.34)] are approximately 1 s and $0.5''$ for interplanetary scintillation and 30 s and 10 arcmin for ionospheric scintillation. Further observations of interplanetary scintillation by Cohen et al. (1967a) showed that the angular size of the radio source 3C273B is smaller than $0.02''$, based on the application of Eq. (14.34). This result, and the long-baseline interferometric results, stimulated the development of VLBI. Interplanetary scintillation can be studied with the modern generation of low-frequency arrays [e.g., Kaplan et al. (2015)].

A comprehensive discussion of the interpretation of interplanetary scintillation can be found in Salpeter (1967), Young (1971), and Scott et al. (1983). For rough calculations, the scattering angle due to the interplanetary medium may be approximated by (Erickson 1964)

$$\theta_s \simeq 50 \left(\frac{\lambda}{p}\right)^2 \ \text{(arcmin)} \ , \tag{14.64}$$

where λ is in meters, and p, the impact parameter, is in solar radii. This relationship is based on measurements taken in 1960–61 at 11-m wavelength for impact parameters between 5 and 50 solar radii. Analysis of VLBI observations at 3.6

and 6 cm obtained in 1991 for a range of impact parameters of 10–50 solar radii led to a model for C_{ne}^2 of the form $C_{ne}^2 = 1.5{\times}10^{14}(r/R_{\rm Sun})^{-3.7}$ (Spangler and Sakurai 1995). Note that the power-law exponent is expected to be about –4 from the elementary consideration that C_{ne}^2 is proportional to the variance of the electron density, which is proportional to the square of the density. For a constant wind speed, the density is proportional to r^{-2}, and hence C_{ne}^2 is proportional to r^{-4}. Deviations from 4 are caused by the radial dependence of the magnetic field strength, which plays a role in driving the turbulence. Integrating C_{ne}^2 along the line of sight, and using Eq. (14.50), we derive an estimate for the scattering angle of $\theta_s = 3100(p/\lambda)^{-2.2}$ arcsec, which is comparable to the result in Eq. (14.64).

The concept that extended sources do not scintillate as much as point sources [see Eq. (14.34)] can be generalized to obtain more information about source structure. We assume that the scintillation is caused by a screen at a distance R from the Earth, as shown in Fig. 14.6, where $R \ll R_s$, and that the intensity at the Earth is $I(x, y)$, where x and y are coordinates in a plane parallel to the screen in Fig. 14.5. The function $\Delta I(x, y)$ is equal to $I(x, y) - \langle I(x, y)\rangle$, where $\langle I(x, y)\rangle$ is the mean intensity. It has a power spectrum $\mathcal{S}_{I0}(q_x, q_y)$ for a point source and $\mathcal{S}_I(q_x, q_y)$ for an extended source, where q_x and q_y are the spatial frequencies (cycles per meter). If the visibility of the source is $\mathcal{V}(q_xR, q_yR)$, then it can be shown (Cohen 1969) that

$$\mathcal{S}_I(q_x, q_y) = \mathcal{S}_{I0}(q_x, q_y)\left|\mathcal{V}(q_xR, q_yR)\right|^2 , \tag{14.65}$$

where q_xR and q_yR correspond to the projected baseline coordinates u and v. The scintillation index of the source m_s is defined by

$$m_s^2 = \frac{\langle \Delta I(x, y)^2\rangle}{\langle I(x, y)\rangle^2} = \frac{1}{\langle I(x, y)\rangle^2}\int_{-\infty}^{\infty}\int_{-\infty}^{\infty}\mathcal{S}_I(q_x, q_y)\, dq_x\, dq_y . \tag{14.66}$$

In principle, $\mathcal{S}_I(q_x, q_y)$ could be computed from the simultaneous measurements of $\Delta I(x, y)$ with a large number of spaced receivers. In practice, the motion of the solar wind sweeps the diffraction pattern across a single telescope so that, from measurements of $\Delta I(t)$, the temporal power spectrum $\mathcal{S}(f)$ can be calculated. If the diffraction pattern moves with velocity v_s in the x direction, then $\mathcal{S}(f)$ can be related to the spatial spectrum since $q_x = f/v_s$:

$$\mathcal{S}(f) = \frac{1}{v_s}\int_{-\infty}^{\infty}\mathcal{S}_I\left(q_x = \frac{f}{v_s}, q_y\right) dq_y . \tag{14.67}$$

In principle, $|\mathcal{V}|^2$ can be recovered from Eq. (14.65) by observing a source over a range of different orientations with respect to the solar wind vector. The situation is entirely analogous to that of lunar occultation observations (Sect. 17.2) except that with lunar occultation observations, the visibility phase can also be obtained. An estimate of the source diameter can be deduced from the width of the temporal power spectrum (Cohen et al. 1967b) or from the scintillation index [Eq. (14.66)] (Little and Hewish 1966).

Table 14.2 Typical values of the effects of the interstellar medium on radiation at 100 MHz

Effect	Equation number	Magnitude[a]	Frequency dependence[b]
Angular broadening[c]	14.43	$0.3''$	ν^{-2}
Pulse broadening[c]	14.32	10^{-4} s	ν^{-4}
Scintillation bandwidth[c]	14.33	10^4 Hz	ν^4
Spectral broadening[c]	—	1 Hz	ν^{-1}
Scintillation timescale[c]	14.31	10 s	ν
Scintillation timescale[d]	—	10^6 s	ν^{-2}
Free-free optical depth	14.22	0.01	ν^{-2}
Faraday rotation	14.71	10 rad	ν^{-2}

Adapted from Cordes (2000).
[a]For a source in the Galactic plane at a distance of 1 kpc. Actual values can differ by an order of magnitude.
[b]Valid for the Gaussian screen model or the power-law turbulence model when $D_\phi(d) \sim d^2$ [see Eq. (14.46)].
[c]Diffractive scattering.
[d]Refractive scattering (see Sect. 14.4.3).

Interplanetary scattering is generally weak, except in directions close to the Sun. An interesting phenomenon is that the scintillation index, m_s, increases monotonically with decreasing impact parameter, reaching $m_s \sim 1$ for small diameter sources around $p \sim 0.1$ and then decreasing for smaller values of p [e.g., Armstrong and Coles (1978), Gapper et al. (1982), Manoharan et al. (1995)]. The effects of refractive scattering (discussed in the next section and in Sect. 15.3), which can be important in the strong scattering regime, have been studied by Narayan et al. (1989).

A substantial effort has been made to study the 3-D characteristics of the interplanetary medium by monitoring the scintillation of radio sources over the past decades. See Manoharan (2012) for results from the Ooty Radio Telescope and Asai et al. (1998) and Tokumaru et al. (2012) for results from the Solar-Terrestrial Environment Laboratory of Nagoya University. Long-term trends are discussed by Janardhan et al. (2015).

14.4 Interstellar Medium

Table 14.2 lists the typical magnitudes and scale sizes of various effects caused by the interstellar medium. These are discussed individually in the following sections.[1]

[1]In this section, we follow the commonly used symbols *DM*, *RM*, and *SM* for dispersion measure, rotation measure, and scintillation measure.

14.4.1 Dispersion and Faraday Rotation

The smooth, ionized component of the interstellar medium of our Galaxy affects propagation by introducing delay and Faraday rotation. The time of arrival of a pulse of radiation, such as that from a pulsar, is

$$t_p = \int_0^L \frac{dy}{v_g} , \tag{14.68}$$

where L is the propagation path, $v_g = cn$ is the group velocity, and n is given by Eq. (14.11), where we neglect the effect of the magnetic field. Differentiation of Eq. (14.68) gives

$$\frac{dt_p}{d\nu} \simeq -\frac{e^2}{4\pi\epsilon_0 mc\nu^3} \int_0^L n_e \, dy . \tag{14.69}$$

The integral of n_e over the path length is called the *dispersion measure*,

$$DM = \int_0^L n_e \, dy , \tag{14.70}$$

which is the same quantity as the total electron content. $dt_p/d\nu$ can be estimated by measuring the time of arrival of pulsar pulses at different frequencies, and the dispersion measure can then be found from Eq. (14.69). If the distance to the pulsar is known, then the average electron density can be calculated. A typical value of $\langle n_e \rangle$ in the plane of our Galaxy is 0.03 cm^{-3} (Weisberg et al. 1980). Alternately, if a pulsar's distance is unknown, it can be estimated from Eq. (14.69) using an estimated average value of n_e.

The magnetic field of the Galaxy causes Faraday rotation of the polarization plane of radiation from extragalactic radio sources. Equation (14.12) can be rewritten

$$\Delta\psi = \lambda^2 RM , \tag{14.71}$$

where RM is the *rotation measure* given by

$$RM = 8.1 \times 10^5 \int_0^L n_e B_\parallel \, dy . \tag{14.72}$$

Here, RM is in radians per square meter, λ is in meters, $B_\parallel$ is the longitudinal component of magnetic field in gauss (1 gauss = 10^{-4} tesla), n_e is in cm^{-3}, and dy is in parsecs (pc) (1 pc $= 3.1 \times 10^{16}$ m). The interstellar magnetic field can be estimated by dividing the rotation measure by the dispersion measure. Typical values of the magnetic field obtained in this way are 2 μG (Heiles 1976). This

procedure underestimates the magnetic field if the field reverses direction along the line of sight. A formula for roughly estimating the rotation measure due to the galactic magnetic field is (Spitzer 1978)

$$RM \simeq -18|\cot b|\cos(\ell - 94^\circ)\ , \tag{14.73}$$

where ℓ and b are the galactic longitude and latitude. Extensive measurements of rotation measure as a function of direction can be found in Oppermann et al. (2012).

Faraday rotation that occurs within a radio source depolarizes the emergent radiation. This depolarization happens because radiation emitted from different depths in the source suffers different amounts of Faraday rotation. Such a source might be a relativistic gas emitting polarized synchrotron radiation immersed in a thermal plasma that causes the Faraday rotation. The degree of polarization of the observed radiation can be succinctly described in a Fourier transform relationship when self-absorption is negligible. We first introduce the function M, the complex degree of linear polarization, defined by

$$M = m_\ell\, e^{j2\psi} = \frac{Q + jU}{I}\ , \tag{14.74}$$

where m_ℓ is the degree of linear polarization, ψ is the position angle of the electric field, and Q, U, and I are the Stokes parameters as defined in Sect. 4.7. If y is the linear distance into the source, $\psi(y)$ is the intrinsic position angle of the radiation at depth y, $j_\nu(y)$ is the volume emissivity of the source, and $\lambda^2\beta(y)$ is the Faraday rotation suffered by radiation emitted at depth y, then the degree of polarization of the observed radiation can be written

$$M(\lambda^2) = \frac{\displaystyle\int_0^\infty m_\ell(y)\, j_\nu(y)\, e^{j2[\psi(y)+\lambda^2\beta(y)]}\, dy}{\displaystyle\int_0^\infty j_\nu(y)\, dy}\ . \tag{14.75}$$

The denominator in Eq. (14.75) is the total intensity. $\beta(y)$ is the Faraday depth, which increases monotonically into the source as long as the sign of the longitudinal magnetic field direction does not change. In any case, we can superpose all the radiation from the same Faraday depth and write the integrals in Eq. (14.75) as a function of β instead of y, yielding

$$M(\lambda^2) = \int_{-\infty}^{\infty} F(\beta) e^{j2\lambda^2\beta}\, d\beta\ , \tag{14.76}$$

where

$$F(\beta) = \frac{m_\ell(y) j_\nu(y) e^{j2\psi(y)}}{\displaystyle\int_0^\infty j_\nu(y)\, dy}\ . \tag{14.77}$$

Thus, $M(\lambda^2)$ and $F(\beta)$ form a Fourier transform pair. $F(\beta)$ is sometimes called the Faraday dispersion function. Unfortunately, $F(\beta)$, in general, cannot be found since M cannot be measured for negative values of λ^2. Because of this difficulty with the Fourier transform, $F(\beta)$ is usually estimated by model fitting. However, if $\psi(y)$ is constant, then $M(-\lambda^2) = M^*(\lambda^2)$, and $F(\beta)$ can be obtained by Fourier transformation.

Consider the result for a simple source model for which m_ℓ, ψ, and j_ν are constant. From Eq. (14.76), we have

$$M(\lambda^2) = M(0)\left[\frac{\sin \lambda^2 RM}{\lambda^2 RM}\right] e^{j\lambda^2 RM} , \tag{14.78}$$

where RM is the Faraday rotation measure through the whole source. If the Faraday rotation originates in front of the radiation source, the complex degree of polarization is

$$M(\lambda^2) = M(0)\, e^{j2\lambda^2 RM} . \tag{14.79}$$

In this case, there is no depolarization, and the Faraday rotation is twice that of Eq. (14.78), in which the source is uniformly distributed throughout the rotation medium. For detailed treatment of intrinsic Faraday rotation, see Burn (1966), Gardner and Whiteoak (1966), and Brentjens and de Bruyn (2005).

14.4.2 Diffractive Scattering

Diffractive interstellar scattering has been extensively investigated by observation of pulsars and compact extragalactic radio sources. For pulsars, the temporal broadening of the pulses [Eq. (14.32)], the decorrelation bandwidth [Eq. (14.33)], and the angular broadening [Eq. (14.27)] can be measured. Interpretation of the measurements in terms of a thin-screen model suggests that $\Delta n_e/n_e \simeq 10^{-3}$ and that the scale size responsible for the scintillation is on the order of 10^{11} cm. The temporal variations or scintillation of the signal from a pulsar are caused by the motions of the observer and the pulsar relative to the quasi-stationary interstellar medium. A measurement of the decorrelation bandwidth can be used to estimate the scattering angle [Eq. (14.33)]. This estimate of the scattering angle and the measurement of the timescale of fading (10^2–10^3 s at 408 MHz) can be used to estimate the relative velocity of the scattering screen by Eq. (14.31). From the relative velocity of the screen, the transverse velocity of the pulsar can be found. Velocities, and thus proper motions, of pulsars estimated in this way (Lyne and Smith 1982) agree with those measured directly with interferometers [see, e.g., Campbell et al. (1996)]. The transverse component of the orbital velocity of a binary pulsar has also been measured (Lyne 1984).

Observations show that the fluctuations in electron density can be described by a power-law spectrum with a power-law exponent of about 3.7 ± 0.3, which is similar to the value of 11/3 for Kolmogorov turbulence (Rickett 1990; Cordes et al. 1986). The power-law spectrum appears to extend over a range of scale sizes from less than 10^{10} cm to more than 10^{15} cm. The inner scale may be set by the proton gyrofrequency ($\sim 10^7$ cm) and the outer scale by the scale height of the Galaxy ($\sim 10^{20}$ cm). Observational evidence for the inner scale is given by Spangler and Gwinn (1990).

Extensive measurements of the angular sizes of extragalactic radio sources have been used to derive an approximate formula for θ_s [see Eq. (14.27)] based on the Gaussian screen model, by Harris et al. (1970), Readhead and Hewish (1972), Cohen and Cronyn (1974), Duffett-Smith and Readhead (1976), and others. This formula is

$$\theta_s \simeq \frac{15}{\sqrt{|\sin b|}} \lambda^2 \text{ (mas)} , \qquad |b| > 15^\circ \tag{14.80}$$

where b is the Galactic latitude and λ is the wavelength in meters. The pulsar data have been interpreted by Cordes (1984) in terms of the power-law model to arrive at approximate formulas for θ_s:

$$\begin{aligned} \theta_s &\simeq 7.5\lambda^{11/5} \text{ (arcsec)} , && |b| \leq 0.^\circ 6 \\ &\simeq 0.5|\sin b|^{-3/5}\lambda^{11/5} \text{ (arcsec)} , && 0.^\circ 6 < |b| < 3^\circ\text{–}5^\circ \\ &\simeq 13|\sin b|^{-3/5}\lambda^{11/5} \text{ (mas)} , && |b| \geq 3^\circ\text{–}5^\circ . \end{aligned} \tag{14.81}$$

The accuracy of the representations in Eqs. (14.81) decreases with decreasing $|b|$. In particular, the scattering angle at low latitudes, $|b| < 1^\circ$, can take on a wide range of values (Cordes et al. 1984). A much more detailed model with 23 parameters characterizing the electron distribution in the Galaxy was constructed by Taylor and Cordes (1993). This model has been superseded by another model called NE2001 (Cordes and Lazio 2002, 2003). They define a scattering measure to characterize the strength of turbulence given by

$$SM = \int_0^L C_n^2 \, dy , \tag{14.82}$$

where C_n^2 is defined in Eq. (14.44). With this definition, the angular broadening of an extragalactic radio source is given by

$$\theta_s \simeq 71 \nu^{-11/5} SM^{3/5} \text{ (mas)} , \tag{14.83}$$

where ν is in GHz. There are several regions in the Galaxy of anomalously high scattering (Cordes and Lazio 2001). The most highly scattered source among them

is a quasar along the line of sight to a galactic HII region known as NGC6334B, which has an angular size of 3″ at 1.5 GHz (Trotter et al. 1998). The apparent sizes of interstellar masers, which are mostly found in the Galaxy at low galactic latitudes, are sometimes set by interstellar scattering (Gwinn et al. 1988).

An example of a compact radio source that suffers a high degree of interstellar scattering is Sagittarius A* at the dynamical center of our Galaxy. This source has an angular size of about 1.0″ at a wavelength of 30 cm (1.5 GHz) [compared with 0.5″ predicted by Eq. (14.81)]. The angular size varies approximately as the wavelength squared over the entire measuring range $\sim$ 0.3–30 cm, as shown in Fig. 14.10. The measurements by Doeleman et al. (2008) show that the intrinsic source size exceeds the scattering size at 1.3 mm. If the scattering can be modeled accurately, as in the case of Sgr A*, then its effects on the image can in principle be removed. The observed visibility $\mathcal{V}_m$ is the true visibility times $\mathcal{V}_s = e^{-D_\phi^2/2}$ [see Eq. (14.48)]. If, for example, $D_\phi = a\lambda^2 d^2$, appropriate if the baseline is less than the inner scale of turbulence, then $\mathcal{V}_s$ is a simple Gaussian function, and the true visibility can be

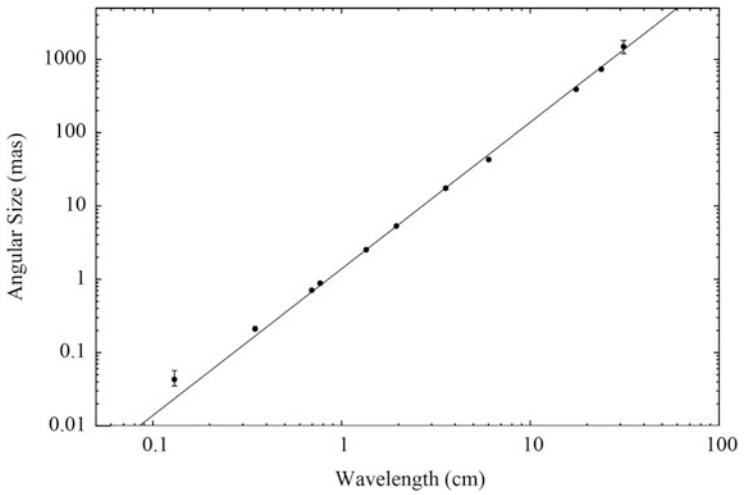

Fig. 14.10 A clear example of interstellar scattering demonstrated by the observed angular size of the compact source in the center of our Galaxy (Sgr A*). The measurements were made with interferometric arrays (Jodrell Bank at the longest two wavelengths, the Event Horizon Telescope at the shortest wavelength, and the VLBA at the intermediate wavelengths). In all cases, the visibility or image data were fitted with Gaussian profiles to determine the major axis (full width at half-maximum). Error bars not visible are smaller than the symbol size. The line is an approximate fit to the data at wavelengths longer than 6 cm and has the form λ^2. The λ-squared dependence suggests that if the scattering is caused by a turbulent medium following the Kolmogorov prescription, it has an inner scale that is longer than the size of the measurement arrays [see Eqs. (14.51) and (14.53)]. Angular sizes for this plot were taken from Davies et al. (1976), Bower et al. (2004, 2006), Shen et al. (2005), and Doeleman et al. (2008). At 0.13 cm, the intrinsic source size exceeds the scattering size. Interstellar scattering was first identified as an image broadening agent in Sgr A* by Davies et al. (1976).

recovered as

$$\mathcal{V} = \mathcal{V}_m/\mathcal{V}_s = \mathcal{V}_m e^{a\lambda^2 d^2/2} \ . \tag{14.84}$$

The success of this inversion clearly depends on the signal-to-noise ratio. Further discussion of "deblurring" techniques can be found in Fish et al. (2014).

14.4.3 Refractive Scattering

The realization by Sieber (1982) that the characteristic periods of amplitude scintillations of pulsars, on timescales of days to months, were correlated with their dispersion measures led Rickett et al. (1984) to the identification of another important scale length in the turbulent interstellar medium, the refractive scale $d_{\rm ref}$. Refractive scattering is important in the strong scattering regime ($d_0 < d_{\rm Fresnel} = \sqrt{\lambda R}$), where d_0 is the diffractive scale size defined by $D_\phi(d_0) = 1$. The refractive scale is the size of the diffractive scattering disk, which is the projection of the cone of scattered radiation on the scattering screen, located a distance R from the observer. The diameter of the diffractive scattering disk is $R\theta_s$. The scattering disk represents the maximum extent on the screen from which radiation can reach the observer. With a power-law distribution of irregularities, it is the irregularities at the maximum allowed scale that have the largest amplitude and are the most influential. Thus, the refractive scale is $d_{\rm ref} \simeq R\theta_s$. Since $\theta_s \simeq \lambda/d_0$, we can write

$$d_{\rm ref} = \frac{\lambda R}{d_0} \ , \tag{14.85}$$

or

$$d_{\rm ref} = \frac{d_{\rm Fresnel}^2}{d_0} \ . \tag{14.86}$$

The scale lengths $d_{\rm ref}$ and d_0 are widely separated. Hence, the timescale associated with scintillation scattering for a screen velocity of v_s, $t_{\rm ref} = d_{\rm ref}/v_s$, is much longer than that associated with diffractive scattering, $t_{\rm dif} = d_0/v_s$. Suppose that a source is observed through a scattering screen located at a distance of 1 kpc, at $b \simeq 20°$, and a wavelength of 0.5 m. For this case, the diffractive scale length is 2×10^9 cm, the Fresnel scale is 4×10^{11} cm, and the refractive scale is 8×10^{13} cm. The typical velocity associated with the interstellar medium is 50 km s^{-1} (the sum of the Earth's orbital motion and the motion of the Sun with respect to the local standard of rest; see Table A10.1). For this velocity, the diffractive and refractive timescales for amplitude scintillation are 6 min and 6 months, respectively. Sgr A*, in addition to its diffractive scattering, also shows the effect of refractive scattering in its visibility function (see Fig. 14.11).

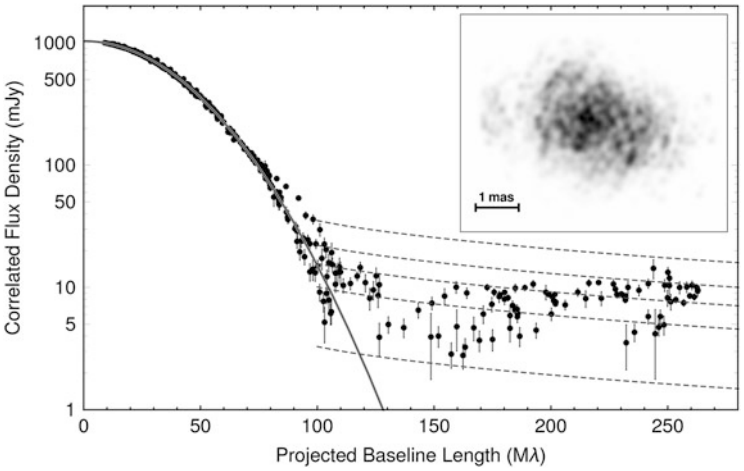

Fig. 14.11 The effect of refractive interstellar scattering on Sgr A* seen on a plot of fringe visibility (correlated flux density) vs. projected baseline at 23.8 GHz. The array consisted of the VLBA augmented with the phased VLA and the GBT. Note the logarithmic flux density scale. The projected baseline has been calculated so as to remove the source elongation. Errors are 1σ values. The solid line through the data shows the visibility model for a Gaussian diffraction-scattered disk with 735-mas diameter (see Fig. 14.10), while the dashed lines above 100 Mλ show the percentage of time the expected visibility for the refractive scattering component should be below the levels indicated for 97, 75, 50, 25, and 3% of the time, respectively. The inset shows a simulated image of Sgr A*, which shows the refractive substructure ($t_{\rm ref} > t_{\rm int} > t_{\rm dif}$) calculated from the algorithm described by Johnson and Gwinn (2015) and smoothed to 0.3 mas. Data from Gwinn et al. (2014).

Refractive scattering is thought to be responsible for the slow amplitude variations observed in some pulsars and quasars at meter and decimeter wavelengths. This realization solved the long-standing problem of understanding the behavior of "long-wavelength variables," which could not be explained by intrinsic variability models based on synchrotron emission. The identification of two scales in the interstellar medium provides strong support for the power-law model. The two scales provide a way of estimating the power-law index, because the relative importance of refractive scattering increases as the power spectrum steepens. It is interesting to note that these two scales arise from a power-law phenomenon, which has no intrinsic scale. The scales are related to the propagation and depend on the wavelength and distance of the screen.

In addition to amplitude scintillation, refractive scattering causes the apparent position of the source to wander with time. The amplitude and timescale are about equal to θ_s and $t_{\rm ref}$, respectively. The character of this wander depends on the power-law index of the fluctuations. Limits on the power-law index have been established from the limits on the amplitude of image wander in the relative positions among clusters of masers (Gwinn et al. 1988).

Rare sudden changes in the intensity of several extragalactic sources, called *Fiedler events*, or *extreme scattering events* (Fiedler et al. 1987), are probably

caused by refractive scattering in the interstellar medium. In the archetypal example, the flux density of the extragalactic source 0954+658 increased by 30% and then dropped by 50% over a period of a month, after which it recovered in symmetric fashion. A large-scale plasma cloud presumably drifted between the source and the Earth, creating flux density changes due to focusing and refraction.

Because there are two timescales associated with strong scattering in the interstellar medium, three distinct data-averaging regimes are important for constructing images from interferometry data obtained on a timescale $t_{\rm int}$. These are: $t_{\rm int} > t_{\rm ref}$ (ensemble average image), $t_{\rm ref} > t_{\rm int} > t_{\rm dif}$ (average image), and $t_{\rm int} < t_{\rm dif}$ (snapshot image). The characteristics of these image regimes are described by Narayan (1992), Narayan and Goodman (1989), and Goodman and Narayan (1989). For ensemble averaging [see Eqs. (14.48) through (14.50)], the image is essentially convolved with the appropriate "seeing" function. An example of an "average" image is shown for the simulation of Sgr A* in Fig. 14.11. For more analysis and simulations of images in various time regimes, see Johnson and Gwinn (2015). The snapshot regime offers intriguing possibilities for image restoration. In this regime, it should be possible to image the source with a resolution of $\lambda/d_{\rm ref}$, which can be very much smaller than that achievable with terrestrial interferometry. In this case, the scattering screen functions as the aperture of the interferometer. Because of the multipath propagation provided by refractive scattering, which brings radiation from widely separated parts of the scattering screen to the observer, the effective baselines can be very large. See Sect. 15.3 for further discussion, including an observation by Wolszczan and Cordes (1987).

Appendix 14.1 Refractive Bending in the Ionosphere

In this appendix, we show that a ray incident on an ionospheric layer will be bent so that it has a smaller zenith angle upon arrival at the Earth's surface, as shown in Fig. 14.2. Application of the law of sines to the two triangles with opening angles θ_1 and θ_2 gives

$$\frac{\sin z_i}{r_0} = \frac{\sin z_0}{r_0 + h_i} \tag{A14.1}$$

and

$$\frac{\sin z_{ir}}{r_0 + h_i + \Delta h} = \frac{\sin z_2}{r_0 + h_i} \,. \tag{A14.2}$$

Snell's law gives the relations

$$n \sin z_{ir} = \sin z_i \tag{A14.3}$$

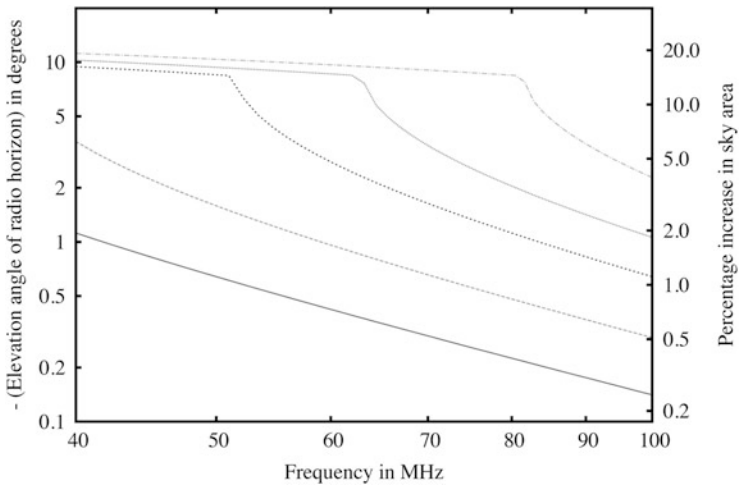

Fig. A14.1 The elevation angle of the radio horizon vs. frequency for various values of electron density in a uniform layer from 200 to 400 km, which approximates the F layer. The densities from the bottom to the top curves are (5, 3, 2, 1, and 0.5) $\times 10^{12}$ m^{-3}, corresponding to plasma frequencies of 20.1, 15.6, 12.7, 9.0, and 6.4 MHz. The knees of the curves (shown only for the higher densities) occur at $\nu \sim 4\nu_p$ [see Eq. (A14.12)]. For frequencies above the knees, the radio horizon is given by Eq. (A14.8) for $z_0 = 90°$. Below the knee, the radio horizon is limited by internal reflection and is given by Eq. (A14.11). From Vedantham et al. (2014). © Royal Astronomical Society, used with permission.

and

$$\sin z_{2r} = n \sin z_2 \ . \tag{A14.4}$$

Combining relations Eqs. (A14.1)–(A14.4) gives

$$\begin{aligned} \sin z_{2r} &= n \sin z_2 \\ &= \frac{r_0 + h_i}{r_0 + h_i + \Delta h}\, n \sin z_{ir} \\ &= \frac{r_0 + h_i}{r_0 + h_i + \Delta h} \sin z_i \\ &= \frac{r_0}{r_0 + h_i + \Delta h} \sin z_0 \ . \end{aligned} \tag{A14.5}$$

Note that z_0 is related to z_{2r} without reference to n. Since $z = z_{2r} + \theta_1 + \theta_2$, the net bending angle is

$$\Delta z = z - z_0 = z_{2r} + \theta_1 + \theta_2 - z_0 \ . \tag{A14.6}$$

Since $\theta_2 = z_{ir} - z_2$,

$$\theta_2 = \sin^{-1}\left\{\frac{1}{n}\frac{r_0}{r_0 + h_i}\sin z_0\right\} - \sin^{-1}\left\{\frac{1}{n}\frac{r_0}{r_0 + h_i + \Delta h}\sin z_0\right\} . \tag{A14.7}$$

Since $\theta_1 = z_0 - z_i$,

$$\theta_1 = z_0 - \sin^{-1}\left\{\frac{r_0}{r_0 + h_i}\sin z_0\right\} . \tag{A14.8}$$

The final result of Δz in terms of $\sin z_0$ is

$$\begin{aligned}\Delta z \; = \sin^{-1}&\left\{\frac{r_0}{r_0 + h_i + \Delta h}\sin z_0\right\} - \sin^{-1}\left\{\frac{r_0}{r_0 + h_i}\sin z_0\right\} \\ &+ \sin^{-1}\left\{\frac{1}{n}\frac{r_0}{r_0 + h_i}\sin z_0\right\} - \sin^{-1}\left\{\frac{1}{n}\frac{r_0}{r_0 + h_i + \Delta h}\sin z_0\right\} .\end{aligned} \tag{A14.9}$$

Note that

$$\Delta z = (z_{2r} - z_2) + (z_{ir} - z_i) . \tag{A14.10}$$

As an example, let us assume that h_i = 300 km, Δh = 200 km, r_0= 6370 km, $n_e = 3 \times 10^{11}$ m^{-3}, and $\nu = 50$ MHz. From Eqs. (14.4) and (14.5), we find that $\nu_p = 4.9$ MHz and $n = 0.9951$. For $z_0 = 75°$, the other angles are $z_i = 67.29°$, $z_{ir} = 67.98°, z_2 = 64.16°, z_{2r} = 63.59°, \theta_1 = 7.71°, \theta_2 = 3.81°, z = 75.11°$, and $\Delta z = 0.11°$. Equation (14.15) gives the same result. This demonstrates the counterintuitive result that the sign of the change in zenith angle is the same for the ionosphere and for the troposphere.

For the case $z_0 = 90°$, the result is $z = 90.22°$, so that the radiation from 0.22° below the horizon can in principle be received.

The phenomenon of internal reflection will occur when $z_{ir} = 90°$. This gives a critical zenith angle, z_c, below which incoming rays will not reach the observer, given by

$$\sin z_c = \frac{r_0 + h_i}{r_0} n . \tag{A14.11}$$

For $z_c = 90°$, the frequency at which this effect limits the incoming zenith angle is

$$\nu \simeq \sqrt{\frac{r_0}{z_{h_i}}}\nu_p \simeq 4\nu_p . \tag{A14.12}$$

The combination of the normal refraction and the critical angle defines the radio horizon. An example of the radio horizon is shown in Fig. A14.1. The radio horizon

may affect studies of the Epoch of Reionization, as described by Vedantham et al. (2014).

Further Reading

Cordes, J.M., Rickett, B.J., and Backer, D.C., Eds., *Radio Wave Scattering in the Interstellar Medium*, Am. Inst. Physics Conf. Proc., **174**, New York (1988)

Lazio, T.J.W., Cordes, J.M., de Bruyn, A.G., and Macquart, J.-P., The Microarcsecond Sky and Cosmic Turbulence, *New Astron. Rev.*, **48**, 1439–1457 (2004)

Narayan, R., The Physics of Pulsar Scintillation, *Phil. Tran. R. Soc. Lond. A*, **341**, 151–165 (1992)

Schunk, R., and Nagy, A., *Ionospheres: Physics, Plasma Physics, and Chemistry*, 2nd ed., Cambridge Univ. Press, Cambridge, UK (2009)

References

Aarons, J., Global Morphology of Ionospheric Scintillations, *Proc. IEEE*, **70**, 360–378 (1982)

Aarons, J., Klobuchar, J.A., Whitney, H.E., Austen, J., Johnson, A.L., and Rino, C.L., Gigahertz Scintillations Associated with Equatorial Patches, *Radio Sci.*, **18**, 421–434 (1983)

Aarons, J., Mendillo, M., Lin, B., Colerico, M., Beach, T., Kintner, P., Scali, J., Reinisch, B., Sales, G., and Kudeki, E., Equatorial F-Region Irregularity Morphology during an Equinoctial Month at Solar Minimum, *Space Science Reviews*, **87**, 357–386 (1999)

Allen, C.W., Interpretation of Electron Densities from Corona Brightness, *Mon. Not. R. Astron. Soc.*, **107**, 426–432 (1947)

Appleton, E.V., and Barnett, M.A.F., On Some Direct Evidence for Downward Atmospheric Reflection of Electric Rays, *Proc. R. Soc. Lond. A*, **109**, 621–641 (1925)

Armstrong, J.W., and Coles, W.A., Interplanetary Scintillations of PSR 0531+21 at 74 MHz, *Astrophys. J.*, **220**, 346–352 (1978)

Asai, K., Kojima, M., Tokumaru, M., Yokobe, A., Jackson, B.V., Hick, P.L., and Manoharan, P.K., Heliospheric Tomography Using Interplanetary Scintillation Observations. 3. Correlation Between Speed and Electron Density Fluctuations in the Solar Wind, *J. Geophys. Res.*, **103**, 1991–2001 (1998)

Bailey, D.K., On a New Method of Exploring the Upper Atmosphere, *J. Terr. Mag. Atmos. Elec.*, **53**, 41–50 (1948)

Beynon, W.J.G., Marconi, Radio Waves, and the Ionosphere, *Radio Sci.*, **10**, 657–664 (1975)

Bilitza, D., International Reference Ionosphere—Status 1995/96, *Adv. Space Res.*, **20**, 1751–1754 (1997)

Booker, H.G., The Use of Radio Stars to Study Irregular Refraction of Radio Waves in the Ionosphere, *Proc. IRE*, **46**, 298–314 (1958)
Booker, H.G., Ratcliffe, J.A., and Shinn, D.H., Diffraction from an Irregular Screen with Applications to Ionospheric Problems, *Philos. Tran. R. Soc. Lond. A*, **242**, 579–607 (1950)
Bougeret, J.-L., King, J.H., and Schwenn, R., Solar Radio Burst and In Situ Determination of Interplanetary Electron Density, *Solar Phys.*, **90**, 401–412 (1984)
Bower, G.C., Falcke, H., Herrnstein, R.M., Zhao, J.-H., Goss, W.M., and Backer, D.C., Detection of the Intrinsic Size of Sagittarius A* Through Closure Ampitude Imaging, *Science*, **304**, 704–708 (2004)
Bower, G.C., Goss, W.M., Falcke, H., Backer, D.C., and Lithwick, Y., The Intrinsic Size of Sagittarius A* from 0.35 to 6 cm, *Astrophys. J. Lett.*, **648**, L127–L130 (2006)
Bracewell, R.N., Eshleman, V.R., and Hollweg, J.V., The Occulting Disk of the Sun at Radio Wavelengths, *Astrophys. J.*, **155**, 367–368 (1969)
Breit, G., and Tuve, M.A., A Test of the Existence of the Conducting Layer, *Phys. Rev.*, **28**, 554–575 (1926)
Brentjens, M.A., and de Bruyn, A.G., Faraday Rotation Measure Synthesis, *Astron. Astrophys.*, **441**, 1217–1228 (2005)
Budden, K.G., *Radio Waves in the Ionosphere*, Cambridge Univ. Press, Cambridge, UK (1961)
Burn, B.J., On the Depolarization of Discrete Radio Sources by Faraday Dispersion, *Mon. Not. R. Astron. Soc.*, **133**, 67–83 (1966)
Campbell, R.M., Bartel, N., Shapiro, I.I., Ratner, M.I., Cappallo, R.J., Whitney, A.R., and Putnam, N., VLBI-Derived Trigonometric Parallax and Proper Motion of PSR B2021+51, *Astrophys. J. Lett.*, **461**, L95–L98 (1996)
Clarke, M., "Two Topics in Radiophysics," Ph.D. thesis, Cambridge Univ. (1964) (see App. II)
Cohen, M.H., High-Resolution Observations of Radio Sources, *Ann. Rev. Astron. Astrophys.*, **7**, 619–664 (1969)
Cohen, M.H., and Cronyn, W.M., Scintillation and Apparent Angular Diameter, *Astrophys. J.*, **192**, 193–197 (1974)
Cohen, M.H., Gundermann, E.J., Hardebeck, H.E., and Sharp, L.E., Interplanetary Scintillations. II. Observations, *Astrophys. J.*, **147**, 449–466 (1967a)
Cohen, M.H., Gundermann, E.J., and Harris, D.E., New Limits on the Diameters of Radio Sources, *Astrophys. J.*, **150**, 767–782 (1967b)
Cordes, J.M., Interstellar Scattering, in *VLBI and Compact Radio Sources*, IAU Symp. 110, Fanti, R., Kellermann, K., and Setti, G., Eds., Reidel, Dordrecht, the Netherlands, (1984), pp. 303–307
Cordes, J.M., Interstellar Scattering: Radio Sensing of Deep Space Through the Turbulent Interstellar Medium, in *Radio Astronomy at Long Wavelengths*, Stone, R.G., Weiler, K.W., Goldstein, M.L., and Bougeret, J.-L., Eds., Geophysical Monograph 119, Am. Geophys. Union, pp. 105–114 (2000)
Cordes, J.M., Ananthakrishnan, S., and Dennison, B., Radio Wave Scattering in the Galactic Disk, *Nature*, **309**, 689–691 (1984)
Cordes, J.M., and Lazio, T.J.W., Anomalous Radio-Wave Scattering from Interstellar Plasma Structures, *Astrophys. J.*, **549**, 997–1010 (2001)
Cordes, J.M., and Lazio, T.J.W., NE2001. I. A New Model for the Galactic Distribution of Free Electrons and Its Fluctuations (2002), astro-ph/0207156
Cordes, J.M., and Lazio, T.J.W., NE2001. II. Using Radio Propagation Data to Construct a Model for the Galactic Distribution of Free Electrons (2003), astro-ph/0301598
Cordes, J.M., Pidwerbetsky, A., and Lovelace, R.V.E., Refractive and Diffractive Scattering in the Interstellar Medium, *Astrophys. J.*, **310**, 737–767 (1986)
Counselman, C.C., III, Kent, S.M., Knight, C.A., Shapiro, I.I., Clark, T.A., Hinteregger, H.F., Rogers, A.E.E., and Whitney, A.R., Solar Gravitational Deflection of Radio Waves Measured by Very-Long-Baseline Interferometry, *Phys. Rev. Lett.*, **33**, 1621–1623 (1974)
Counselman, C.C., III, and Rankin, J.M., Density of the Solar Corona from Occultations of NP0532, *Astrophys. J.*, **175**, 843–856 (1972)
Crane, R.K., Ionospheric Scintillation, *Proc. IEEE*, **65**, 180–199 (1977)

Daniell, R.E., Brown, L.D., Anderson, D.N., Fox, M.W., Doherty, P.H., Decker, D.T., Sojka, J.J., and Schunk, R.W., Parameterized Ionospheric Model: A Global Ionospheric Parameterization Based on First Principles Models, *Radio Sci.*, **30**, 1499–1510 (1995)

Davies, K., *Ionospheric Radio Propagation*, National Bureau of Standards Monograph 80, U.S. Government Printing Office, Washington, DC (1965)

Davies, R.D., Walsh, D., and Booth, R.S., The Radio Source at the Galactic Nucleus, *Mon. Not. R. Astron. Soc.*, **177**, 319–333 (1976)

Doeleman, S.S., Weintroub, J., Rogers, A.E.E., Plambeck, R., Freund, R., Tilanus, R.P.J., Friberg, P., Ziurys, L.M., Moran, J.M., Corey, B., and 18 coauthors, Event-Horizon-Scale Structure in the Supermassive Black Hole Candidate at the Galactic Center, *Nature*, **455**, 78–80 (2008)

Duffett-Smith, P.J., and Readhead, A.C.S., The Angular Broadening of Radio Sources by Scattering in the Interstellar Medium, *Mon. Not. R. Astron. Soc.*, **174**, 7–17 (1976)

Erickson, W.C., The Radio-Wave Scattering Properties of the Solar Corona, *Astrophys. J.*, **139**, 1290–1311 (1964)

Erickson, W.C., Perley, R.A., Flatters, C., and Kassim, N.E., Ionospheric Corrections for VLA Observations Using Local GPS Data, *Astron. Astrophys.*, **366**, 1071–1080 (2001)

Evans, J.V., Theory and Practice of Ionosphere Study by Thomson Scatter Radar, *Proc. IEEE*, **57**, 496–530 (1969)

Evans, J.V., and Hagfors, T., *Radar Astronomy*, McGraw-Hill, New York (1968)

Fejer, B.G., and Kelley, M.C., Ionospheric Irregularities, *Rev. Geophys. Space Sci.*, **18**, 401–454 (1980)

Fiedler, R.L., Dennison, B., Johnston, K.J., and Hewish, A., Extreme Scattering Events Caused by Compact Structures in the Interstellar Medium, *Nature*, **326**, 675–678 (1987)

Fish, V.L., Johnson, M.D., Lu, R.-S., Doeleman, S.S., Bouman, K.L., Zoran, D., Freeman, W.T., Psaltis, D., Narayan, R., Pankratius, V., Broderick, A.E., Gwinn, C.R., and Vertatschitch, L.E., Imaging an Event Horizon: Mitigation of Scattering Toward Sagittarius A*, *Astrophys. J.*, **795**:134 (7pp) (2014)

Fomalont, E.B., and Sramek, R.A., A Confirmation of Einstein's General Theory of Relativity by Measuring the Bending of Microwave Radiation in the Gravitational Field of the Sun, *Astrophys. J.*, **199**, 749–755 (1975)

Frail, D.A., Kulkarni, S.R., Nicastro, L., Ferocl, M., and Taylor, G.B., The Radio Afterglow from the γ-Ray Burst of 8 May 1997, *Nature*, **389**, 261–263 (1997)

Gapper, G.R., Hewish, A., Purvis, A., and Duffett-Smith, P.J., Observing Interplanetary Disturbances from the Ground, *Nature*, **296**, 633–636 (1982)

Gardner, F.F., and Whiteoak, J.B., The Polarization of Cosmic Radio Waves, *Ann. Rev. Astron. Astrophys.*, **4**, 245–292 (1966)

Goodman, J., and Narayan, R., The Shape of a Scatter-Broadened Image: II. Interferometric Visibilities, *Mon. Not. R. Astron. Soc.*, **238**, 995–1028 (1989)

Gupta, Y., Pulsars and Interstellar Scintillations, in *Pulsar Astrometry—2000 and Beyond*, M. Kramer, N. Wex, and R. Wielebinski, Eds., Astron. Soc. Pacific Conf. Ser., **202**, 539–544 (2000)

Gwinn, C.R., Kovalev, Y.Y., Johnson, M.D., and Soglasnov, V.A., Discovery of Substructure in the Scatter-Broadened Image of Sgr A*, *Astrophys. J. Lett.*, **794**:L14 (5pp) (2014)

Gwinn, C.R., Moran, J.M., Reid, M.J., and Schneps, M.H., Limits on Refractive Interstellar Scattering Toward Sagittarius B2, *Astrophys. J.*, **330**, 817–827 (1988)

Hagfors, T., The Ionosphere, in *Methods of Experimental Physics*, Vol. 12, Part B *(Astrophysics: Radio Telescopes)*, M. L. Meeks, Ed., Academic Press, New York (1976), pp. 119–135

Harris, D.E., Zeissig, G.A., and Lovelace, R.V., The Minimum Observable Diameter of Radio Sources, *Astron. Astrophys.*, **8**, 98–104 (1970)

Heiles, C., The Interstellar Magnetic Field, *Ann. Rev. Astron. Astrophys.*, **14**, 1–22 (1976)

Helmboldt, J.F., Drift-Scan Imaging of Traveling Ionospheric Disturbances with the Very Large Array, *Geophys. Res. Lett.*, **41**, 4835–4843 (2014)

Helmboldt, J.F., Lane, W.M., and Cotton, W.D., Climatology of Midlatitude Ionospheric Disturbances from the Very Large Array Low-Frequency Sky Survey, *Radio Sci.*, **37**, RS5008 (19pp) (2012)

Hewish, A., The Diffraction of Galactic Radio Waves as a Method of Investigating the Irregular Structure of the Ionosphere, *Proc. R. Soc. Lond. A*, **214**, 494–514 (1952)

Hewish, A., Scott, P.F., and Wills, D., Interplanetary Scintillation of Small Diameter Radio Sources, *Nature*, **203**, 1214–1217 (1964)

Hey, J.S., Parsons, S.J., and Phillips, J.W., Fluctuations in Cosmic Radiation at Radio Frequencies, *Nature*, **158**, 234 (1946)

Ho, C.M., Mannucci, A.J., Lindqwister, U.J., Pi, X., and Tsurutani, B.T., Global Ionospheric Perturbations Monitored by the Worldwide GPS Network, *Geophys. Res. Lett.*, **23**, 3219–3222 (1996)

Ho, C.M., Wilson, B.D., Mannucci, A.J., Lindqwister, U.J., and Yuan, D.N., A Comparative Study of Ionospheric Total Electron Content Measurements Using Global Ionospheric Maps of GPS, TOPEX Radar, and the Bent Model, *Radio Sci.*, **32**, 1499–1512 (1997)

Hocke, K., and Schlegel, K., A Review of Atmospheric Gravity Waves and Travelling Ionospheric Disturbances: 1982–1995, *Ann. Geophysicae*, **14**, 917–940 (1996)

Holt, E.H., and Haskell, R.E., *Foundations of Plasma Dynamics*, Macmillan, New York (1965), p. 254

Hunsucker, R.D., Atmospheric Gravity Waves Generated in the High-Latitude Ionosphere: A Review, *Rev. Geophys. Space Phys.*, **20**, 293–315 (1982)

Jaeger, J.C., and Westfold, K.C., Equivalent Path and Absorption for Electromagnetic Radiation in the Solar Corona, *Aust. J. Phys.*, **3**, 376–386 (1950)

Janardhan, P., Bisoi, S.K., Ananthakrishnan, S., Tokumaru, M., Fujiki, K., Jose, L., and Sridharan, R., A Twenty-Year Decline in Solar Photospheric Magnetic Fields: Inner-Heliospheric Signatures and Possible Implications, *J. Geophys. Res.: Space Phys.*, **120**, 5306–5317 (2015)

Johnson, M.D., and Gwinn, C.R., Theory and Simulations of Refractive Substructure in Resolved Scatter-Broadened Images, *Astrophys. J.*, **805**:180 (15pp) (2015)

Kaplan, D.L., Tingay, S.J., Manoharan, P.K., Macquart, J.-P., Hancock, P., Morgan, J., Mitchell, D.A., Ekers, R.D., Wayth, R.B., Trott, C., and 27 coauthors, Murchison Widefield Array Observations of Anomalous Variability: A Serendipitous Nighttime Detection of Interplanetary Scintillation, *Astrophys. J. Lett.*, **809**:L12 (7pp) (2015)

Kaplan, G.H., Josties, F.J., Angerhofer, P.E., Johnston, K.J., and Spencer, J.H., Precise Radio Source Positions from Interferometric Observations, *Astron. J.*, **87**, 570–576 (1982)

Kundu, M.R., *Solar Radio Astronomy*, Wiley-Interscience, New York (1965), p. 104

Lawrence, R.S., Little, C.G., and Chivers, H.J.A., A Survey of Ionospheric Effects upon Earth-Space Radio Propagation, *Proc. IEEE*, **52**, 4–27 (1964)

Lazio, T.J.W., and Cordes, J.M., Hyperstrong Radio-Wave Scattering in the Galactic Center. I. A Survey for Extragalactic Sources Seen through the Galactic Center, *Astrophys. J. Suppl.*, **118**, 201–216 (1998)

Leblanc, Y., Dulk, G.A., and Bougeret, J.-L., Tracing the Electron Density from the Corona to 1 AU, *Solar Phys.*, **183**, 165–180 (1998)

Little, L.T., and Hewish, A., Interplanetary Scintillation and Relation to the Angular Structure of Radio Sources, *Mon. Not. R. Astron. Soc.*, **134**, 221–237 (1966)

Loi, S.T., Murphy, T., Bell, M.E., Kaplan, D.L., Lenc, E., Offinga, A.R., Hurley-Walker, N., Bernardi, G., Bowman, J.D., Briggs, F., and 32 coauthors, Quantifying Ionospheric Effects on Time-Domain Astrophysics with the Murchison Widefield Array, *Mon. Not. R. Astron. Soc.*, **453**, 2731–2746 (2015a)

Loi, S.T., Murphy, T., Cairns, I.H., Menk, F.W., Waters, C.L., Erickson, P.J., Trott, C.M., Hurley-Walker, N., Mortan, J., Lenc, E., and 31 coauthors, Real-Time Imaging of Density Ducts Between the Plasmasphere and Ionosphere, *Geophys. Res. Lett.*, **42**, 3707–3714 (2015b)

Lyne, A.G., Orbital Inclination and Mass of the Binary Pulsar PSR0655+64, *Nature*, **310**, 300–302 (1984)

Lyne, A.G., and Smith, F.G., Interstellar Scintillation and Pulsar Velocities, *Nature*, **298**, 825–827 (1982)

Mannucci, A.J., Wilson, B.D., Yuan, D.N., Ho, C.H., Lindqwister, U.J., and Runge, T.F., A Global Mapping Technique for GPS-Derived Ionospheric Total Electron Content Measurements, *Radio Sci.*, **33**, 565–582 (1998)

Manoharan, P.K., Three-Dimensional Evolution of Solar Wind During Solar Cycles 22–24, *Astrophy. J.*, **751**:128 (13pp) (2012)

Manoharan, P.K., Ananthakrishnan, S., Dryer, M., Detman, T.R., Leinbach, H., Kojima, M., Watanabe, T., and Kahn, J., Solar Wind Velocity and Normalized Scintillation Index from Single-Station IPS Observations, *Solar Phys.*, **156**, 377–393 (1995)

Mathur, N.C., Grossi, M.D., and Pearlman, M.R., Atmospheric Effects in Very Long Baseline Interferometry, *Radio Sci.*, **5**, 1253–1261 (1970)

Mercier, R.P., Diffraction by a Screen Causing Large Random Phase Fluctuations, *Proc. R. Soc. Lond. A*, **58**, 382–400 (1962)

Moran, J.M., The Effects of Propagation on VLBI Observations, in *Very Long Baseline Interferometry: Techniques and Applications*, Felli, M., and Spencer, R.E., Eds., Kluwer, Dordrecht, the Netherlands, (1989), pp. 47–59

Narayan, R., From Scintillation Observations to a Model of the ISM–The Inverse Problem, in *Radio Wave Scattering in the Interstellar Medium*, Cordes, J.M., Rickett, B.J., and Backer, D.C., Eds., Am. Inst. Physics Conf. Proc., **174**, New York (1988), pp. 17–31

Narayan, R., The Physics of Pulsar Scintillation, *Phil. Tran. R. Soc. Lond. A*, **341**, 151–165 (1992)

Narayan, R., Anantharamaiah, K.R., and Cornwell, T.J., Refractive Radio Scintillation in the Solar Wind, *Mon. Not. R. Astron. Soc.*, **241**, 403–413 (1989)

Narayan, R., and Goodman, J., The Shape of a Scatter-Broadened Image: I. Numerical Simulations and Physical Principles, *Mon. Not. R. Astron. Soc.*, **238**, 963–994 (1989)

Oppermann, N., Junklewitz, H., Robbers, G., Bell, M.R., Enßlin, T.A., Bonafede, A., Braun, R., Brown, J.C., Clarke, T.E., Feain, I.J., and 21 coauthors, An Improved Map of the Galactic Faraday Sky, *Astron. Astrophys.*, **542**, A93 (14pp) (2012)

Pi, X., Mannucci, A.J., Lindqwister, U.J., and Ho, C.M., Monitoring of Global Ionospheric Irregularities Using the Worldwide GPS Network, *Geophys. Res. Lett.*, **24**, 2283–2286 (1997)

Ratcliffe, J.A., Some Aspects of Diffraction Theory and Their Application to the Ionosphere, *Rep. Prog. Phys.*, **19**, 188–267 (1956)

Ratcliffe, J.A., *The Magneto-Ionic Theory and Its Application to the Ionosphere*, Cambridge Univ. Press, Cambridge, UK (1962)

Readhead, A.C.S., and Hewish, A., Galactic Structure and the Apparent Size of Radio Sources, *Nature*, **236**, 440–443 (1972)

Rickett, B.J., Radio Propagation Through the Turbulent Interstellar Medium, *Ann. Rev. Astron. Astrophys.*, **28**, 561–605 (1990)

Rickett, B.J., Coles, W.A., and Bourgois, G., Slow Scintillation in the Interstellar Medium, *Astron. Astrophys.*, **134**, 390–395 (1984)

Roberts, D.H., Rogers, A.E.E., Allen, B.R., Bennet, C.L., Burke, B.F., Greenfield, P.E., Lawrence, C.R., and Clark, T.A., Radio Interferometric Detection of a Traveling Ionospheric Disturbance Excited by the Explosion of Mt. St. Helens, *J. Geophys. Res.*, **87**, 6302–6306 (1982)

Rogers, A.E.E., Bowman, J.D., Vierinen, J., Monsalve, R., and Mozdzen, T., Radiometric Measurements of Electron Temperature and Opacity of Ionospheric Perturbations, *Radio Sci.*, **50**, 130–137 (2015)

Ros, E., Marcaide, J.M., Guirado, J.C., Sardón, E., and Shapiro, I.I., A GPS-Based Method to Model the Plasma Effects in VLBI Observations, *Astron. Astrophys.*, **356**, 357–362 (2000)

Salpeter, E.E., Interplanetary Scintillations. I. Theory, *Astrophys. J.*, **147**, 433–448 (1967)

Scheuer, P.A.G., Amplitude Variations in Pulsed Radio Sources, *Nature*, **218**, 920–922 (1968)

Schunk, R., and Nagy, A., *Ionospheres: Physics, Plasma Physics, and Chemistry*, 2nd ed., Cambridge Atmospheric and Space Science Series, Cambridge Univ. Press, Cambridge, UK, (2009)

Scott, S.L., Coles, W.A., and Bourgois, G., Solar Wind Observations Near the Sun Using Interplanetary Scintillation, *Astron. Astrophys.*, **123**, 207–215 (1983)

Shapiro, I.I., Estimation of Astrometric and Geodetic Parameters, in *Methods of Experimental Physics*, Vol. 12, Part C *(Astrophysics: Radio Observations)*, Meeks, M.L., Ed., Academic Press, New York (1976), pp. 261–276

Shen, Z.-Q., Lo, K.Y., Liang, M.-C., Ho, P.T.P. and Zhao, J.-H., A Size of $\sim$ 1 AU for the Radio Source Sgr A* at the Center of the Milky Way, *Nature*, **438**, 62–64 (2005)

Sieber, W., Causal Relationship Between Pulsar Long-Term Intensity Variations and the Interstellar Medium, *Astron. Astrophys.*, **113**, 311–313 (1982)

Smart, W.M., *Textbook on Spherical Astronomy*, 6th ed., revised by Green, R.M., Cambridge Univ. Press, Cambridge, UK (1977)

Smith, F.G., Little, C.G., and Lovell, A.C.B., Origin of the Fluctuations in the Intensity of Radio Waves from Galactic Sources, *Nature*, **165**, 422–424 (1950)

Spangler, S.R., and Gwinn, C.R., Evidence for an Inner Scale to the Density Turbulence in the Interstellar Medium, *Astrophys. J. Lett.*, **353**, L29–L32 (1990)

Spangler, S.R., and Sakurai, T., Radio Interferometry of Solar Wind Turbulence from the Orbit of Helios to the Solar Corona, *Astrophys. J.*, **445**, 999–1061 (1995)

Spitzer, L., *Physical Processes in the Interstellar Medium*, Wiley-Interscience, New York (1978), p. 65

Spoelstra, T.A.T., The Influence of Ionospheric Refraction on Radio Astronomy Interferometry, *Astron. Astrophys.*, **120**, 313–321 (1983)

Spoelstra, T.A.T., and Kelder, H., Effects Produced by the Ionosphere on Radio Interferometry, *Radio Sci.*, **19**, 779–788 (1984)

Sukumar, S., Ionospheric Refraction Effects on Radio Interferometer Phase, *J. Astrophys. Astr.*, **8**, 281–294 (1987)

Taylor, J.H., and Cordes, J.M., Pulsar Distances and the Galactic Distribution of Free Electrons, *Astrophys. J.*, **411**, 674–684 (1993)

Tokumaru, M., Kojima, M., and Fujiki, K., Long-Term Evolution in the Global Distribution of Solar Wind Speed and Density Fluctuations During 1997–2009, *J. Geophys. Res.*, **117**, A06108 (14 pp) (2012)

Trotter, A.S., Moran, J.M., and Rodríguez, L.F., Anisotropic Radio Scattering of NGC6334B, *Astrophys. J.*, **493**, 666–679 (1998)

Vedantham, H.K., Koopmans, L.V.E., de Bruyn, A.G., Wijnholds, A.J., Ciardi, B., and Brentjens, M.A., Chromatic Effects in the 21-cm Global Signal from the Cosmic Dawn, *Mon. Not. R. Astron. Soc.*, **437**, 1056–1059 (2014)

Weinberg, S., *Gravitation and Cosmology: Principles and Applications of the General Theory of Relativity*, Wiley, New York (1972), p. 188

Weisberg, J.M., Rankin, J., and Boriakoff, V., HI Absorption Measurements of Seven Low Latitude Pulsars, *Astron. Astrophys.*, **88**, 84–93 (1980)

Winterhalter, D., Gosling, J.T., Habbal, S.R., Kurth, W.S., and Neugebauer, M., Eds., *Solar Wind Eight*, Proc. 8th Int. Solar Wind Conf., Vol. 382, Am. Inst. Physics, New York (1996)

Wolszczan, A., and Cordes, J.M., Interstellar Interferometry of the Pulsar PSR 1237+25, *Astrophys. J. Lett.*, **320**, L35–L39 (1987)

Yeh, K.C., and Liu, C.H., Radio Wave Scintillations in the Ionosphere, *Proc. IEEE*, **70**, 324–360 (1982)

Young, A.T., Interpretation of Interplanetary Scintillations, *Astrophys. J.*, **168**, 543–562 (1971)